

Please see our responses below which are highlighted in red.

## Review #1

In general, the authors have satisfactorily addressed reviewer comments. I recommend that the authors consider the below comments and also recommend that the authors review the manuscript in careful detail to ensure that the manuscript uses accurate and precise language on specific details (E.g., along the lines as described in the paragraph below for the Introductory paragraph)

Thank you for your comments.

The first paragraph of the introduction should be edited for clarity and accuracy. 1) NO reaction with HO<sub>2</sub> or RO<sub>2</sub> does not “accelerate” O<sub>3</sub> production, it is the only major known reacting leading to net production of NO<sub>2</sub> and subsequently O<sub>3</sub> in the troposphere. 2) lightning NO<sub>x</sub> is not biogenic, but geogenic. 3) NO<sub>x</sub> does not ‘transform’ in to HNO<sub>3</sub>, but rather NO<sub>2</sub> reacts with OH or N<sub>2</sub>O<sub>5</sub> reacts in aqueous solution to form HNO<sub>3</sub>.

These have been clarified. The revised paragraph is below:

“Nitrogen oxides (NO<sub>x</sub> ≡ NO+NO<sub>2</sub>) are a group of reactive trace gases that are toxic to human health and can be converted in the atmosphere into other noxious chemical species. In the presence of abundant volatile organic compounds and strong sunlight, NO<sub>x</sub> can participate in a series of chemical reactions to generate a net accumulation of O<sub>3</sub>, another toxic air pollutant with a longer atmospheric lifetime. NO<sub>x</sub> also participates in a series of reactions to create HNO<sub>3</sub>, a key contributor to acid rain, and particulate nitrate (NO<sub>3</sub><sup>-</sup>), a component of fine particulate matter (PM<sub>2.5</sub>), an additional health hazard. There are some natural emissions of NO<sub>x</sub> (e.g., lightning), but the majority of the NO<sub>x</sub> emissions are from anthropogenic sources (van Vuuren et al., 2011).”

The authors indicated in their response that there was no NO<sub>y</sub> simulation results archived (comment for P10L32), for the purpose of analyzing NO<sub>x</sub> lifetime in the simulation, but they added a comparison of model output to NO<sub>y</sub> observations in the revised manuscript. Please, consider a comparison of NO<sub>x</sub>:NO<sub>y</sub> in model as well as has been shown for NO<sub>x</sub>:NO<sub>y</sub> in observations.

We misunderstood the original comment as a request for data from the process analysis tool, which was not output in this simulation. We have added the NO<sub>2</sub>:NO<sub>y</sub> model vs. observation comparison, and re-formatted Figure 9. Both simulations captured the NO<sub>2</sub>:NO<sub>y</sub> ratio fairly well; neither simulation performed any better than the other. A sentence on this is now included in Section 3.7 and shown below:

“The NO<sub>2</sub>-NO<sub>y</sub> partitioning is captured well by both model simulations, and there is no significant change in the NO<sub>2</sub>-NO<sub>y</sub> ratio when using increased NO<sub>x</sub> emissions.”

P13 L19 – L30 of annotated revised manuscript: The discussion of NO<sub>2</sub> lifetime should be edited for clarity before publication. To be an accurate means of inverting NO<sub>x</sub> emissions in the EMG method, the effective lifetime derived from NO<sub>2</sub> column measurements must be directly, physically related to the PBL NO<sub>x</sub> lifetime (The EMG method accounts for background NO<sub>2</sub> and NO<sub>2</sub>:NO<sub>x</sub> ratio). I.e., PBL NO<sub>x</sub> MASS = NO<sub>x</sub> EMISSIONS \* NO<sub>x</sub> PHOTOCHEMICAL LIFETIME. I understand that any error in wind direction results in the inference of a biased NO<sub>x</sub> lifetime value, but that doesn’t mean that the gradient has no bearing on the rate at which NO<sub>x</sub> is being removed from the boundary layer. The question

instead should be “what factors affect the spatial pattern of NO<sub>2</sub> column downwind of a city that should be accounted for when estimating the NO<sub>x</sub> photochemical lifetime.

The authors should also note here that there are oscillating thermally-driven wind flows in the basin that are challenging to resolve and may also lead to biased lifetime calculation. In the current version of the manuscript, these effects are only discussed in the conclusions section (P15 L16-25 of annotated revised manuscript). I would also disagree with the authors: there would be systematic impacts of local circulations on the spatial pattern of NO<sub>2</sub> columns that would not necessarily be captured in the larger scale synoptic flow patterns. During night, air would flow downslope and out over the Yellow Sea. During daytime, the flow would reverse to the E. In general, the large scale flows during this time of year would be northwesterly. I don't expect the authors to fully account for these but to acknowledge that they may exist.

This paragraph in Section 3.6.2 has now been revised. We have also removed the statement in the discussion suggesting that there is no consistent bias in the top-down NO<sub>x</sub> emissions calculation.

We have now more explicitly stated that heterogeneous topography and oscillating thermally driven wind flows are effects that may bias the effective photochemical lifetime calculation. We partially accounted for this bias by only selecting days with strong synoptic winds; on days with faster winds speeds, the sea & mountain breeze effects are secondary to the synoptic flow. The last two sentences of the Section 3.6.2 paragraph have been removed. Please see the updated paragraph below:

“It should be noted that the NO<sub>2</sub> photochemical lifetime derived here is a fundamentally different quantity than the NO<sub>2</sub> lifetime observed by in situ measurements (de Foy et al., 2014; Lu et al., 2015) or derived by model simulations (Lamsal et al., 2010). This is because the lifetime calculation is extremely sensitive to the accuracy of the wind direction (de Foy et al., 2014) and spatial pattern of the emissions. Inaccuracies in the wind fields introduce noise that shorten the tail of the fit. As a result, NO<sub>2</sub> photochemical lifetimes derived here are considered “effective” photochemical lifetimes and are generally shorter than the tropospheric column NO<sub>2</sub> lifetimes derived by model simulations (Lamsal et al., 2010). NO<sub>x</sub> sources at the outer portions of urban areas will lead to an artificially longer NO<sub>2</sub> lifetime. This partially compensates for the bias introduced by the wind direction. The heterogeneous topography and oscillating thermally driven wind flows (such as the Yellow Sea breeze) in the Seoul metropolitan area are effects that may bias the effective photochemical lifetime calculation. We partially account for this bias by only selecting days with strong winds (>3 m/s); on days with faster winds speeds, the sea & mountain breeze effects are secondary to the synoptic flow.”

P13 L19 – L30: “It should be noted that the NO<sub>2</sub> photochemical lifetime derived here is a fundamentally different quantity than the NO<sub>2</sub> lifetime observed by in situ measurements (de Foy et al., 2014; Lu et al., 2015) or derived by model simulations (Lamsal et al., 2010). This is because the lifetime calculation is extremely sensitive to the accuracy of the wind direction (de Foy et al., 2014). Inaccuracies in the wind fields introduce noise that shorten the tail of the fit. As a result, NO<sub>2</sub> photochemical lifetimes derived here are considered “effective” photochemical lifetimes and are universally shorter than the tropospheric column NO<sub>2</sub> lifetimes derived by model simulations (Lamsal et al., 2010). NO<sub>x</sub> sources at the outer portions of urban areas will lead to an artificially longer NO<sub>2</sub> lifetime. This partially 25 compensates for the bias introduced by the wind direction. The effective photochemical lifetime is also different from the NO<sub>2</sub> lifetime derived by in situ measurements of NO<sub>2</sub> at the surface or within the

boundary layer. In the boundary layer, NO<sub>2</sub> is consumed faster yielding lifetimes that are shorter than the lifetimes based on tropospheric columns (Nunnermacker et al., 2007).”

## Review #2

The revised manuscript by Goldberg et al. does an admirable job of addressing reviewer questions and following up on most reviewer suggestions. This includes additional simulations (longer simulations, additional emissions perturbation experiment) and evaluations (e.g., NO<sub>y</sub>), so the changes go beyond just text revisions, for which the authors are commended. Overall the paper is much improved, and I recommend it for publication in ACP, following some revisions to the text to address two points that could use further clarification, described below. Addressing these will not likely warrant further peer review.

Thank you for your comments.

Comments:

I appreciate the additional detail added in section 2.1.1 regarding how WRF-Chem profile biases are corrected. The details state that in each grid box, this bias is corrected via comparison to in situ aircraft observations. Are there unique profiles from aircraft measurements in each grid box though? I don't think so, as that would have required a lot of aircraft spirals. So, how is it determined which aircraft profile to use to correct the model values in each grid box? If comparing to the profiles measured by the aircraft throughout the entire “Seoul” or “mainland” transects (ie shown in Fig 5), how representative are these of model profiles in individual grid boxes? Some additional explanation and discussion of these issues is warranted.

We use a campaign mean comparison over all land-based areas and scale all modeled profiles by this ratio. As you correctly identified, there are not enough measurements in any one grid box to scale each individual model grid cell differently. Without more measurements, we are unsure how using a campaign-long mean comparison instead of a daily or location-specific comparison will affect the AMF calculation. This is beyond the scope of this paper. The revised sentence is below:

“We use a campaign mean comparison over all land-based areas (34° – 38° N, 126° – 130° E) and scale all modeled profiles in this box by this ratio; there are not enough measurements in any one grid box to scale each individual model grid cell differently.”

Despite an attempt at clarifying in the revisions and response, I still don't follow what the authors are trying to demonstrate with discussion of NO<sub>2</sub> emissions diurnal profiles and Figure 4. They are not clear regarding what they are suggesting. Do they think the diurnal variability in the model is incorrect? It seems though this is not an issue, as they show the emission rate at the model overpass time is representative of the 24 hr average. Do they suspect this is fortuitous? I'm not sure what they are suggesting as to why this agreement would explain a model underestimate of NO<sub>2</sub> columns. Further, the inclusion of a plot of diurnal variability of NO<sub>x</sub> emissions in the US has yet to be strongly connected to whatever argument is being attempted here. Diurnal profiles of NO<sub>x</sub> emissions are different in different parts of the world — I'm not sure including a figure adds much to that statement. Thus, I still contend that Fig 4 and associated discussion be removed. Lastly, “temporalization” is not a word — suggest “temporal allocation” or “diurnal variability.” And on this topic, the authors are mistaken in their response that they are the first to consider that model errors in diurnal variability could bias inversions

based on LEO satellites; rather, this is a common concern and a justification for the upcoming GEO satellites.

The temporal allocation of bottom-up emissions inventories can be a very significant source of uncertainty when using LEO satellites that only observe the mid-afternoon emissions rate. As you correctly identified, this was always a concern in the NO<sub>x</sub> remote sensing community that uses LEO satellites, but we have now put a loose bounds on this uncertainty. We are showing that there are scenarios in which the temporal allocation can be up to 35% different! The magnitude of this difference was much larger than we thought. We are not suggesting that the Korean emissions inventory should have the diurnal profile of the US or vice versa, but instead that there are scenarios in which the temporal allocation can vary widely. This further justifies the use of GEO satellites, perhaps even more than before.

We have modified the discussion in Section 3.3 to better clarify our thoughts and changed the word “temporalization” to temporal allocation. Please see below:

“Third, the temporal allocation of bottom-up emissions inventories can be a very significant source of uncertainty (Mues et al., 2014). The temporal allocation of the bottom-up Korean NO<sub>x</sub> emissions is such that the early afternoon rate during the OMI overpass time (between 12:00 – 14:00 local time) is approximately equal to 24-hour averaged rate (Figure 4). For comparison, in the eastern US, the early afternoon emission rate is 1.35 larger than the 24-hour averaged emission rate. Thus, there are scenarios in which the temporal allocation can be up to 35% different in the mid-afternoon during the OMI overpass time. We are not suggesting that the Korean emissions inventory should have the diurnal profile of the US or vice versa, but instead that there are scenarios in which the temporal allocation can vary widely. This substantiates the future use of geostationary satellites to better constrain this temporal allocation uncertainty. Lastly, the remaining difference will likely be due to an underestimate in the emissions inventory.”

# A top-down assessment using OMI NO<sub>2</sub> suggests an underestimate in the NO<sub>x</sub> emissions inventory in Seoul, South Korea during KORUS-AQ

5 Daniel L. Goldberg<sup>\*,1,2</sup>, Pablo E. Saide<sup>3</sup>, Lok N. Lamsal<sup>4,5</sup>, Benjamin de Foy<sup>6</sup>, Zifeng Lu<sup>1,2</sup>, Jung-Hun Woo<sup>7</sup>, Younha Kim<sup>7</sup>, Jinseok Kim<sup>7</sup>, Meng Gao<sup>8</sup>, Gregory Carmichael<sup>9</sup>, and David G. Streets<sup>1,2</sup>

<sup>1</sup>Energy Systems Division, Argonne National Laboratory, Argonne, IL 60439 USA

<sup>2</sup>Consortium for Advanced Science and Engineering, University of Chicago, Chicago, IL 60637, USA

10 <sup>3</sup>Department of Atmospheric and Oceanic Sciences, Institute of the Environment and Sustainability, University of California – Los Angeles, Los Angeles, CA 90095, USA

<sup>4</sup>Goddard Earth Sciences Technology and Research, Universities Space Research Association, Columbia, MD 21046, USA

<sup>5</sup>NASA Goddard Space Flight Center, Code 614, Greenbelt, MD 20771, USA

15 <sup>6</sup>Department of Earth and Atmospheric Sciences, Saint Louis University, St. Louis, MO 63108, USA

<sup>7</sup>Konkuk University, 05029 Seoul, South Korea

<sup>8</sup>School of Engineering and Applied Sciences, Harvard University, Cambridge, MA 02138, USA

<sup>9</sup>Department of Chemical and Biochemical Engineering, University of Iowa, Iowa City, IA 52242, USA

*Correspondence to:* Daniel L. Goldberg ([dgoldberg@anl.gov](mailto:dgoldberg@anl.gov))

20 **Abstract.** In this work, we investigate the NO<sub>x</sub> emissions inventory in Seoul, South Korea using a regional Ozone Monitoring Instrument (OMI) NO<sub>2</sub> product derived from the standard NASA product. We first develop a regional OMI NO<sub>2</sub> product by re-calculating the air mass factors using a high-resolution (4 × 4 km<sup>2</sup>) WRF-Chem model simulation, which better captures the NO<sub>2</sub> profile shapes in urban regions. We then apply a model-derived spatial averaging kernel to further downscale the retrieval and account for the sub-pixel variability. These two modifications yield OMI NO<sub>2</sub> values in the regional product that are 1.37 larger in the Seoul metropolitan region and >2 times larger near substantial point sources. These two modifications also yield an OMI NO<sub>2</sub> product that is in better agreement with the Pandora NO<sub>2</sub> spectrometer measurements acquired during the Korea U.S.-Air Quality (KORUS-AQ) field campaign. NO<sub>x</sub> emissions are then derived for the Seoul metropolitan area during the KORUS-AQ field campaign using a top-down approach with the standard and regional NASA OMI NO<sub>2</sub> products. We first apply the top-down approach to a model simulation to ensure that the method is appropriate: the WRF-Chem simulation utilizing the bottom-up emission inventory yields a NO<sub>x</sub> emission rate of 227 ± 94 kton/yr, while the bottom-up inventory itself within a 40 km radius of Seoul yields a NO<sub>x</sub> emission rate of 198 kton/yr. Using the top-down approach on the regional OMI NO<sub>2</sub> product, we derive the NO<sub>x</sub> emissions rate from Seoul to be 484 ± 201 kton/yr, and a 353 ± 146 kton/yr NO<sub>x</sub> emissions rate using the standard NASA OMI NO<sub>2</sub> product. This suggests an underestimate of 53% and 36% in the bottom-up inventory using the regional and standard NASA OMI NO<sub>2</sub> products respectively. To supplement this finding, we compare the NO<sub>2</sub> and NO<sub>y</sub> simulated by WRF-Chem to observations of the same quantity acquired by aircraft and find a model underestimate. When NO<sub>x</sub> emissions in the WRF-Chem model are increased by a factor of 2.13 in the Seoul metropolitan area, there is better agreement with KORUS-AQ aircraft observations and the re-calculated OMI NO<sub>2</sub> tropospheric columns. Finally, we show that by using a WRF-Chem simulation with an updated emissions inventory to re-calculate the AMF, there are small differences (~8%) in OMI NO<sub>2</sub> compared to using the original WRF-Chem simulation to derive the AMF. This suggests that changes in model resolution have a

larger effect on the AMF calculation than modifications to the Korean emissions inventory. Although the current work is focused on South Korea using OMI, the methodology developed in this work can be applied to other world regions using TROPOMI and future satellite datasets (e.g., GEMS and TEMPO) to produce high-quality region-specific top-down NO<sub>x</sub> emission estimates.

## 1 Introduction

Nitrogen oxides ( $\text{NO}_x \equiv \text{NO} + \text{NO}_2$ ) are a group of reactive trace gases that are toxic to human health and can ~~transform be converted~~ in the atmosphere into other noxious chemical species. In the presence of abundant volatile organic compounds and strong sunlight,  $\text{NO}_x$  can participate in a series of chemical reactions to ~~accelerate the production generate a net accumulation~~ of  $\text{O}_3$ , another toxic air pollutant with a longer atmospheric lifetime.  ~~$\text{NO}_x$  can also transform into particulate nitrate, a component of fine particulate matter ( $\text{PM}_{2.5}$ ), an additional health hazard. When fully oxidized in the atmosphere,  $\text{NO}_x$  transforms into  $\text{NO}_x$  also participates in a series of reactions to create~~  $\text{HNO}_3$ , a key contributor to acid rain, ~~and particulate nitrate ( $\text{NO}_3^-$ ), a component of fine particulate matter ( $\text{PM}_{2.5}$ ), an additional health hazard.~~ There are some ~~biogenic/natural~~ emissions of  $\text{NO}_x$  (e.g., lightning), but the majority of the  $\text{NO}_x$  emissions are from anthropogenic sources (van Vuuren et al., 2011).

There is a rich legacy of  $\text{NO}_2$  measurements by remote sensing instruments (Burrows et al., 1999). One of these instruments is the Dutch-Finnish Ozone Monitoring Instrument (OMI), which measures the absorption of solar backscatter in the UV-visible spectral range.  $\text{NO}_2$  can be observed from space because it has strong absorption features within the 400 – 465 nm wavelength region (Vandaele et al., 1998). By comparing observed spectra with a reference spectrum, the amount of  $\text{NO}_2$  in the atmosphere between the instrument in low-earth orbit and the surface can be derived; this technique is called differential optical absorption spectroscopy (DOAS) (Platt, 1994).

Tropospheric  $\text{NO}_2$  column contents from OMI have been used to estimate  $\text{NO}_x$  emissions from various areas around the globe (Streets et al., 2013; Miyazaki et al., 2017) including North America (Boersma et al., 2008; Lu et al., 2015), Asia (Zhang et al., 2008; Han et al., 2015; Kuhlmann et al., 2015; Liu et al., 2017), the Middle East (Beirle et al., 2011), and Europe (Huijnen et al., 2010; Curier et al., 2014). It has also been used to produce and validate  $\text{NO}_x$  emission estimates from sectors such as soil (Hudman et al., 2010; Vinken et al., 2014a; Rasool et al., 2016), lightning (Allen et al., 2012; Liaskos et al., 2015; Pickering et al., 2016; Nault et al., 2017), power plants (de Foy et al., 2015), aircraft (Pujadas et al., 2011), marine vessels (Vinken et al., 2014b; Boersma et al., 2015), and urban centers (Lu et al., 2015; Canty et al., 2015; Souri et al., 2016).

With a pixel resolution varying from  $13 \times 24 \text{ km}^2$  to  $26 \times 128 \text{ km}^2$ , the OMI sensor was developed for global to regional scale studies rather than for individual urban areas. Even at the highest spatial resolution of  $13 \times 24 \text{ km}^2$ , the sensor has difficulty observing the fine structure of  $\text{NO}_2$  plumes at or near the surface (e.g., highways, power plants, factories, etc.) (Chen et al., 2009; Ma et al., 2013; Flynn et al., 2014), which are often less than 10 km in width (Heue et al., 2008). This can lead to a spatial averaging of pollution (Hilboll et al., 2013). A temporary remedy, until higher spatial resolution satellite instruments are operational, is to use a regional air quality simulation to estimate the sub-pixel variability of OMI pixels. Kim et al. (2016) utilize the spatial variability in a regional air quality model to spatially downscale OMI  $\text{NO}_2$  measurements using a spatial averaging kernel. The spatial averaging kernel technique has shown to increase the OMI  $\text{NO}_2$  signal within urban areas, which is in better agreement with observations in these regions (Goldberg et al., 2017).

Furthermore, the air mass factor and surface reflectance used in obtaining the global OMI NO<sub>2</sub> retrievals are at a coarse spatial resolution (Lorente et al. 2017; Kleipool et al., 2008). While appropriate for a global operational retrieval, this is known to cause an underestimate in the OMI NO<sub>2</sub> signal in urban regions (Russell et al., 2011). The air mass factors in [the operational OMI NO<sub>2</sub> retrieval](#) are calculated using NO<sub>2</sub> profile shapes that are provided at a 1.25° × 1° spatial resolution in the NASA product (Krotkov et al. 2017) and 2° × 3° spatial resolution in the DOMINO product (Boersma et al., 2011). Developers of the NASA product provide scattering weights and additional auxiliary information so that users can develop their own tropospheric vertical column product a posteriori (Lamsal et al. 2015). Several users have re-calculated the air mass factor using a regional air quality model (Russell et al., 2011; Kuhlmann et al. 2015; Lin et al., 2015; Goldberg et al., 2017; [Laughner et al., 2019](#)), which can better capture the NO<sub>2</sub> profile shapes in urban regions. Other techniques to improve the air mass factor involve correcting for the surface pressure in mountainous terrain (Zhou et al., 2009) and accounting for small-scale heterogeneities in surface reflectance (Zhou et al., 2010; Vasilkov et al., 2017). These a posteriori products have better agreement with ground-based spectrometers measuring tropospheric vertical column contents (Goldberg et al., 2017). When available, observations from aircraft can constrain the NO<sub>2</sub> profile shapes used in the air mass factor calculation (Goldberg et al., 2017).

In this paper, we apply both techniques (the spatial averaging kernel and an air mass factor adjustment) to develop a regional OMI NO<sub>2</sub> product for South Korea. We then use the regional product with only the air mass factor adjustment to derive NO<sub>x</sub> emission estimates for the Seoul metropolitan area using [a statistical fit to](#) an exponentially modified Gaussian (EMG) function (Beirle et al., 2011; Valin et al., 2013; de Foy et al., 2014; Lu et al., 2015); the methodology is described in-depth in Section 2.5.

## 2 Methods

### 2.1 OMI NO<sub>2</sub>

OMI has been operational on NASA's Earth Observing System (EOS) Aura satellite since October 2004 (Levelt et al., 2006). The satellite follows a sun-synchronous, low-earth (705 km) orbit with an equator overpass time of approximately 13:45 local time. OMI measures total column amounts in a 2600 km swath divided into 60 unequal area "field-of-views", or pixels. At nadir (center of the swath), pixel size is 13 × 24 km<sup>2</sup>, but at the swath edges, pixels can be as large as 26 × 128 km<sup>2</sup>. In a single orbit, OMI measures approximately 1650 swaths and achieves daily global coverage over 14 – 15 orbits (99 minutes per orbit). Since June 2007, there has been a partial blockage of the detector's full field of view, which has limited the number of valid measurements by blocking consistent rows of data; this is known in the community as the row anomaly (Dobber et al., 2008): <http://projects.knmi.nl/omi/research/product/rowanomaly-background.php>.

OMI measures radiance data between the instrument's detector and the Earth's surface. Comparison of these measurements with a reference spectrum (i.e., DOAS technique), enables the calculation of the total slant column density (SCD), which represents an integrated trace gas abundance from the sun to the surface and back to the instrument's detector, passing through the atmosphere twice. For tropospheric air quality studies, vertical column



density (VCD) data are more ~~useful~~relevant. This is done by subtracting the stratospheric slant column from the total (tropospheric + stratospheric) slant column and dividing by the tropospheric air mass factor (AMF), which is defined as the ratio of the SCD to the VCD, as shown in Eq. (1):

$$VCD_{trop} = \frac{SCD_{total} - SCD_{strat}}{AMF_{trop}}, \text{ where } AMF_{trop} = \frac{SCD_{trop}}{VCD_{trop}} \quad (1)$$

5 The tropospheric AMF has been derived to be a function of the optical atmospheric/surface properties (viewing and solar angles, surface reflectivity, cloud radiance fraction, and cloud height) and a priori profile shape (Palmer et al., 2001; Martin et al., 2002) and can be calculated as follows (Lamsal et al., 2014) in Eq. (2):

$$AMF_{trop} = \frac{\sum_{n=surface}^{tropopause} SW_n \times x_n}{\sum_{n=surface}^{tropopause} x_n} \quad (2)$$

10 where  $x$  is the partial column. The optical atmospheric/surface properties in the NASA retrieval are characterized by the scattering weight and are calculated by a forward radiative transfer model (TOMRAD), which are output as a look-up table. The scattering weights are then adjusted real-time depending on observed viewing angles, surface albedo, cloud radiance fraction, and cloud pressure.

15 ~~For this study, w~~We follow previous studies (e.g., Palmer et al., 2001, Martin et al., 2002, Boersma et al., 2011, Bucsele et al., 2013) and assume that scattering weights and trace gas profile shapes are independent. The a priori trace gas profile shapes ( $x_a$ ) must be provided by a model simulation. In an operational setting, NASA uses a monthly-averaged and year-specific Global Model Initiative (GMI) global simulation with a spatial resolution of  $1.25^\circ \text{ lon} \times 1^\circ \text{ lat}$  ( $\sim 110 \text{ km} \times 110 \text{ km}$  in the mid-latitudes) to provide the a priori profile shapes. For this study, we derive tropospheric VCDs using a priori  $\text{NO}_2$  profile shapes from a regional WRF-Chem simulation. A full description of this methodology can be found in Goldberg et al. (2017); it is also described in brief in section 2.1.1. We filter the 20 Level 2 OMI  $\text{NO}_2$  data to ensure only valid pixels are used. Daily pixels with solar zenith angles  $\geq 80^\circ$ , cloud radiance fractions  $\geq 0.5$ , or surface albedo  $\geq 0.3$  are removed as well as the five largest pixels at the swath edges (i.e., pixel numbers 1 – 5 and 56 – 60). Finally, we remove any pixel flagged by NASA including pixels with NaN values, ‘XTrackQualityFlags’  $\neq 0$  or 255 (RA flag), or ‘VcdQualityFlags’  $> 0$  and least significant bit  $\neq 0$  (ground pixel flag).

### 2.1.1 OMI-WRF-Chem $\text{NO}_2$

25 We modify the air mass factor in the OMI  $\text{NO}_2$  retrieval based on the vertical profiles from a high spatial ( $4 \times 4 \text{ km}^2$ ) resolution WRF-Chem simulation. The vertical profiles are scaled based on a comparison with in situ aircraft observations; this accounts for any consistent biases in the model simulation. We use a campaign mean comparison over all land-based areas ( $34^\circ - 38^\circ \text{ N}$ ,  $126^\circ - 130^\circ \text{ E}$ ) and scale all modeled profiles in this box by this ratio; there are not enough measurements in any one grid box to scale each individual model grid cell differently. For example, 30 if the aircraft observations during the campaign show that mean  $\text{NO}_2$  concentrations between 0 - 500 m are low by 50%, then we scale all of the modeled  $\text{NO}_2$  in this altitude bin by this same amount. To re-calculate the air mass factor

for each OMI pixel, we first compute sub-pixel air mass factors for each WRF-Chem model grid cell, using the same method as outlined in Goldberg et al. (2017). The sub-pixel air mass factor for each WRF-Chem grid cell is a function of the modelled NO<sub>2</sub> profile shape and the scattering weight calculated by a radiative transfer model. We then average all sub-pixel air mass factors within an OMI pixel (usually 10-100) to generate a single tropospheric air mass factor for each individual OMI pixel. This new air mass factor is used to convert the total slant column into a total vertical column using Equation 1. Model outputs were sampled at the local time of OMI overpass. For May 2016, we used daily NO<sub>2</sub> profiles and terrain pressures (e.g., (Zhou et al., 2009, Laughner et al., 2016)) to re-calculate the AMF. For other months and years, we used May 2016 monthly mean values of NO<sub>2</sub> and tropopause pressures for the a priori profiles, which are used in the calculation of the AMF.

Once the tropospheric vertical column of each OMI pixel was re-calculated, the product was oversampled (de Foy et al., 2009; Russell et al., 2010) for April – June over a 3-year period (2015-2017; 9 months total). During this timeframe, there are approximately 9 valid OMI NO<sub>2</sub> pixels per month over any given location on the Korean peninsula. In the top-down emissions derivation, we use all nine-months of OMI data for the analysis.

## 2.2 NO<sub>2</sub> observations during KORUS-AQ

We use in situ NO<sub>2</sub> observations from the KORUS-AQ field campaign to test the regional satellite product. KORUS-AQ was a joint Korea-US field experiment designed to better understand the trace gas and aerosol composition above the Korean peninsula using aircrafts, ground station networks, and satellites. The campaign took place between May 1, 2016 and June 15, 2016 and measurements were primarily focused in the Seoul Metropolitan Area. In this paper, we utilize data acquired by the ground-based Pandora spectrometer network, the thermally dissociated laser-induced fluorescence NO<sub>2</sub> instrument on DC-8 aircraft, and the chemiluminescence NO<sub>y</sub> instrument on the DC-8 aircraft (NO<sub>y</sub> = NO + NO<sub>2</sub> + HNO<sub>3</sub> + 2×N<sub>2</sub>O<sub>5</sub> + peroxy nitrates + alkyl nitrates + ...). KORUS-AQ observations were retrieved from the online data archive: <http://www-air.larc.nasa.gov/cgi-bin/ArcView/korusaq>. A further description of this field campaign can be found in the KORUS-AQ White Paper ([https://espo.nasa.gov/korus-aq/content/KORUS-AQ\\_Science\\_Overview\\_0](https://espo.nasa.gov/korus-aq/content/KORUS-AQ_Science_Overview_0)).

### 2.2.1 Pandora NO<sub>2</sub> data

Measurements of total column NO<sub>2</sub> from the Pandora instrument (Herman et al., 2009) are used to evaluate the OMI NO<sub>2</sub> satellite products. The Pandora instrument is a stationary, ground-based, sun-tracking spectrometer, which measures direct sunlight in the UV-Visible spectral range (280-525 nm) with a sampling period of 90 seconds. The Pandora spectrometer measures total column NO<sub>2</sub> using a DOAS technique similar to OMI. A distinct advantage of the Pandora instrument is that it does not require complex assumptions for converting slant columns into vertical columns, compared to zenith sky measurements (e.g., MAX-DOAS). [The spatial and temporal variation of NO<sub>2</sub> columns in Korea as observed by Pandora has been documented elsewhere \(Chong et al., 2018; Herman et al., 2018\).](#)

In our comparison, valid OMI NO<sub>2</sub> pixels are matched spatially and temporally to Pandora total column NO<sub>2</sub> observations. To smooth the data and eliminate brief small-scale plumes that would be undetectable by a satellite, we average the Pandora observations over a two hour period ( $\pm$  one hour of the overpass time) before matching to the OMI NO<sub>2</sub> data (Goldberg et al., 2017). During May 2016, there were seven Pandora NO<sub>2</sub> spectrometers operating during the experiment (five instruments were situated within the Seoul metropolitan area and their locations are shown in Figure 5); this corresponded to fifty instances in which valid Pandora NO<sub>2</sub> observations matched valid OMI NO<sub>2</sub> column data.

### 2.2.2 DC-8 aircraft data

We compare the model simulation to in situ NO<sub>2</sub> data gathered by the UC-Berkeley Cohen group (Thornton et al., 2000; Day et al, 2002) on the DC-8 aircraft. The instrument quantifies NO<sub>2</sub> via laser-induced fluorescence at 585 nm. This instrument does not have the same positive bias as chemiluminescence NO<sub>2</sub> detectors, so there is no need to modify NO<sub>2</sub> concentrations by applying an empirical equation (e.g., Lamsal et al., 2008). We also compare the model simulation to chemiluminescence NO<sub>y</sub> data gathered by the NCAR Weinheimer group (Ridley et al., 2004)

We utilize one-minute averaged DC-8 data from all fourteen flights during May – June 2016. A typical flight path included several low-altitude spirals over the Seoul Metropolitan Area and a long-distance transect over the Korean peninsula or the Yellow Sea. One-minute averaged data is already pre-generated in the data archive. Hourly output from the model simulation is spatially and temporally matched to the observations. We then bin the data into different altitude ranges for our comparison.

### 2.3 WRF-Chem model simulation

For the high-resolution OMI NO<sub>2</sub> product, we use a regional simulation of the Weather Research & Forecasting (Skamarock et al., 2008) coupled to Chemistry (WRF-Chem) (Grell et al., 2005) in forecast mode prepared for flight planning during the KORUS-AQ field campaign. The forecast simulations were performed daily and used National Centers for Environmental Prediction Global Forecast System (<https://rda.ucar.edu/datasets/ds084.6/>) meteorological initial and boundary conditions from the 06 UTC cycle. Initial conditions for aerosols and gases were obtained from the previous forecasting cycle, while Copernicus Atmosphere Monitoring Service (Inness et al., 2015) forecasts were used as boundary conditions. WRF-Chem was configured with two domains, with 20 km and 4 km grid-spacing. The 20 km domain included the major sources for trans-boundary pollution impacting the Korean peninsula (deserts in China and Mongolia, wild-fires in Siberia and anthropogenic sources from China). The 4 km domain provided a high-resolution simulation where detailed local sources could be modeled and where the KORUS-AQ flight tracks were contained. The inner domain was started 18 hours after the outer domain, and was simulated for 33 hours (00UTC from day 1 to 9 UTC of day 2 of the forecast); output was saved hourly. The last 24 hours of each inner domain daily forecast over the course of KORUS-AQ were selected to allow spin-up from the outer domain and were used in the analysis presented here.

WRF-Chem was configured with 4 bin MOSAIC aerosols (Zaveri et al., 2008), a reduced hydrocarbon trace gas chemical mechanism (Pfister et al., 2014) including simplified secondary organic aerosol formation (Hodzic and Jimenez, 2011), and with capabilities to assimilate satellite aerosol optical depth both from low-earth orbiting and geostationary satellites (Saide et al., 2013, 2014).

## 5 2.4 Emission Inventory

The WRF-Chem simulation was driven by emissions developed by Konkuk University. Monthly emissions for South Korea were developed using the projected 2015 Korean national emissions inventory, Clean Air Policy Support System (CAPSS) provided by the National Institute of Environmental Research of Korea and with enhancements by Konkuk University, which primarily include the addition of new power plants. The projected CAPSS 2015 emissions were estimated based on CAPSS 2012 and 3-year growth factors. Since the base year of the inventory is 2012, observed emissions from the post-2013 Large Point Source inventory were not included. Emissions from China and North Korea were taken from the Comprehensive Regional Emissions for Atmospheric Transport Experiments (CREATE) v3.0 emissions inventory. In order to project the year 2010 emissions to 2015, the latest energy statistics from the International Energy Agency (<http://www.iaea.org/weo2017/>) and the China Statistical Yearbook 2016 (<http://www.stats.gov.cn/tjsj/ndsj/2016/indexeh.htm>) were used to update the growth of fuel activities. In addition, the new emissions control policies in China, which were compiled by the International Institute for Applied Systems Analysis, were applied to consider efficiencies of emissions control (van der A et al., 2017).

Emissions were first processed to the monthly time-scale at a spatial resolution of 3 km in South Korea and 0.1° for the rest of Asia using SMOKE-Asia (Woo et al., 2012). Information from GIS, such as population, road network, and land cover, were applied to generate gridded emissions from the region-based (17 metropolitan and provincial boundaries of South Korea) emissions. The GIS-based population and regional boundary data compiled by the Ministry of Interior and Safety (<http://www.mois.go.kr/frt/sub/a05/totStat/>), and land cover data compiled by the Ministry of Environment (<https://egis.me.go.kr/>) were used to generate population and land cover based spatial surrogates. The Road and Railroad network data compiled by The Korea Transport Institute were used to generate spatial surrogates for onroad and nonroad emissions (<https://www.koti.re.kr/>). The emissions were downscaled temporally from monthly to hourly and spatially re-allocated to 4 km over South Korea and 20 km over the rest of East Asia using the University of Iowa emission pre-processor (EPRES).

Biogenic emissions are included using the on-line Model of Emissions of Gases and Aerosols from Nature (MEGAN) model version 2; there are no NO<sub>x</sub> emissions from MEGAN. For this simulation, the lightning NO<sub>x</sub> parameterization was turned off. For wildfires we used the Quick Fire Emissions Dataset (QFED2), but there were only isolated, small fires in South Korea during this timeframe.

## 2.5 Exponentially Modified Gaussian Fitting Method

An exponentially modified Gaussian (EMG) function is fit to a collection of NO<sub>2</sub> plumes observed from OMI in order to determine the NO<sub>2</sub> burden and lifetime from the Seoul metropolitan area. The original methodology, proposed by Beirle et al. (2011), involves the fitting of OMI NO<sub>2</sub> line densities to an EMG function. OMI NO<sub>2</sub> line densities are the integral of OMI NO<sub>2</sub> retrieval perpendicular to the path of the plume; the units are mass per distance. We define integration length scale as the across plume width. The across plume width is dependent on the NO<sub>2</sub> plume size and can vary between 10 km (for small point sources) to 240 km (for large urban areas). Visual inspection of the rotated oversampled OMI NO<sub>2</sub> plumes is the best way to determine the spatial extent of the emission sources (Lu et al. 2015).

The EMG model is expressed as Equation (3):

$$OMI\ NO_2\ Line\ Density = \alpha \left[ \frac{1}{x_o} \exp\left(\frac{\mu}{x_o} + \frac{\sigma^2}{2x_o^2} - \frac{x}{x_o}\right) \Phi\left(\frac{x-\mu}{\sigma} - \frac{\sigma}{x_o}\right) \right] + \beta \quad (3)$$

where  $\alpha$  is the total number of NO<sub>2</sub> molecules observed near the hotspot, excluding the effect of background NO<sub>2</sub>,  $\beta$ ;  $x_o$  is the e-folding distance downwind, representing the length scale of the NO<sub>2</sub> decay;  $\mu$  is the location of the apparent source relative to the city center;  $\sigma$  is the standard deviation of the Gaussian function, representing the Gaussian smoothing length scale;  $\Phi$  is the cumulative distribution function. Using the ‘curvefit’ function in IDL, we determine the five unknown parameters:  $\alpha$ ,  $x_o$ ,  $\sigma$ ,  $\mu$ ,  $\beta$  based on the independent (distance; x) and dependent (OMI NO<sub>2</sub> line density) variables.

Using the mean zonal wind speed,  $w$ , of the NO<sub>2</sub> line density domain, the mean effective NO<sub>2</sub> lifetime  $\tau_{effective}$  and the mean NO<sub>x</sub> emissions can be calculated from the fitted parameters  $x_o$  and  $\alpha$ . The wind speed and direction are obtained from the ERA-Interim re-analysis project (Dee et al., 2011), instead of the WRF simulation because the WRF simulation is a forecast. We use the averaged wind fields of the bottom eight levels of the re-analysis (i.e., from the surface to ~500 m). Only days in which the wind speeds are > 3 m/s are included in this analysis, because NO<sub>2</sub> decay under this condition is dominated by chemical removal, not variability in the winds (de Foy et al., 2014). The factor of 1.33 is the mean column-averaged NO<sub>x</sub> / NO<sub>2</sub> ratio in the WRF-Chem model simulation for the Seoul metropolitan area during the mid-afternoon. The NO<sub>x</sub> / NO<sub>2</sub> ratio is time-dependent, spatially varying and is primarily a function of the localized j(NO<sub>2</sub>) and O<sub>3</sub> concentration.

$$NO_x\ Emissions = 1.33 \left( \frac{\alpha}{\tau_{effective}} \right), \text{ where } \tau_{effective} = \frac{x_o}{w} \quad (4)$$

The NO<sub>2</sub> plume concentration is a function of the emission source strength, wind speed, and wind direction. Originally, the method separated all NO<sub>2</sub> plumes by wind direction, and fit an EMG function to NO<sub>2</sub> in eight wind directions (Beirle et al., 2011; Ialongo et al., 2014; Liu et al., 2016). Newer methodologies rotate the plumes so that all plumes are in the same direction (Valin et al., 2013; de Foy et al., 2014; Lu et al., 2015). This process increases the signal-to-noise ratio and generates a more robust fit. In this work, we filter OMI NO<sub>2</sub> data and rotate the NO<sub>2</sub> plumes and as

described in Lu et al. (2015), so that all plumes are decaying in the same direction. We rotate the retrieval based on the re-analyzed 0-500 m wind speed direction from the ERA-Interim. In doing so, we develop a re-gridded satellite product in an x-y coordinate system, in which the urban plume is aligned along the x-axis. Following de Foy et al. (2014) and Lu et al. (2015), we only use days in which the ERA-Interim wind speeds are  $> 3$  m/s because there is more direct plume transport and less plume meandering on days with stronger winds; this yields more robust  $\text{NO}_x$  emission estimates. We fit an EMG function to the line density as function of the horizontal distance. This yields a single value at each point along the x-direction.

### 3 Results

In this section, we describe the regional high-resolution satellite product and our validation efforts. All OMI  $\text{NO}_2$  results presented here are vertical column densities. First, we show a continental snapshot of OMI  $\text{NO}_2$  (OMI-Standard) over East Asia using the standard NASA product. Then, we show a regional NASA OMI  $\text{NO}_2$  satellite product (OMI-Regional) using AMFs generated from the WRF-Chem a priori  $\text{NO}_2$  profiles. We compare the OMI-Regional product with  $\text{NO}_2$  VCDs from the original WRF-Chem simulation. We evaluate the OMI-Regional product by comparing to KORUS-AQ observations. Finally, we use the OMI-Standard and OMI-Regional products to estimate  $\text{NO}_x$  emissions from the Seoul metropolitan area.

#### 3.1 OMI $\text{NO}_2$ in East Asia

Oversampled OMI  $\text{NO}_2$  for May – September 2015 – 2017 (15 months total) in East Asia and the 4 km WRF-Chem model domain are shown in Figure 1. The OMI  $\text{NO}_2$  signals in East Asia over major metropolitan areas are 3 to 5 times larger than over similarly sized cities in the US (Krotkov et al., 2016). This is in despite of recent  $\text{NO}_x$  reductions in China since 2011 (de Foy et al., 2016; Souri et al., 2017; Zheng et al., 2018). OMI has observed a recent decrease in the  $\text{NO}_2$  burden in the immediate Seoul, South Korea metropolitan area, but an increase in areas just outside the city center (Duncan et al., 2016). Oversampled values greater than  $8 \times 10^{15}$  molecules per  $\text{cm}^2$  are still consistently seen in East Asia, while they are non-existent in the US during the warm season.

#### 3.2 Calculation of new OMI tropospheric column $\text{NO}_2$

In Figure 2, we plot the OMI-Standard and OMI-Regional products over South Korea. The left panels are identical and show the OMI-Standard product for Apr – Jun 2015 – 2017. The top center panel shows a regional product in which only the air mass factor correction is applied (AMF). The bottom center panel shows a regional product in which the air mass factor correction and spatial averaging kernel are applied (AMF+SK). The regional product yields larger OMI  $\text{NO}_2$  values throughout the majority of the Korean peninsula. Areas near major cities (e.g. Seoul), power plants, steel mills, and cement kilns have OMI  $\text{NO}_2$  values that are  $>1.25$  times larger in the regional AMF product and  $>2$  times larger in the regional AMF+SK product. There are two reasons for the larger OMI  $\text{NO}_2$  signals: the air mass factors in polluted regions are now smaller (Russell et al., 2011; Goldberg et al., 2017) and the spatial weighting kernel allocates a large portion of the OMI  $\text{NO}_2$  signal into a smaller region (Kim et al., 2016).

### 3.3 OMI-Regional vs. WRF-Chem

We now compare the OMI-Regional product to tropospheric vertical columns from the WRF-Chem model simulation directly. In Figure 3, we compare the regional satellite product (AMF+SK) to the WRF-Chem simulation over the Korean peninsula. In most areas, the modeled tropospheric column NO<sub>2</sub> is of smaller magnitude than inferred by the satellite. In the area within 40 km of the Seoul city center, modeled tropospheric vertical columns are 44% smaller than observed tropospheric vertical column in the regional AMF+SK product. We posit four reasons as to why the model simulation calculates columns that are consistently smaller. First, our WRF-Chem simulation uses a reduced hydrocarbon gas-phase chemical mechanism. This fast-calculating mechanism implemented in WRF-Chem for regional climate assessments (Pfister et al., 2014) and used during KORUS-AQ for forecasting does not quickly recycle alkyl nitrates back to NO<sub>2</sub>; this will cause NO<sub>2</sub> to be too low. While an underestimate of the chemical conversion to NO<sub>2</sub> in WRF-Chem is a contributor to the underestimate, it likely does not account for the entire discrepancy; Canty et al., (2015) suggests that by shortening the lifetime of alkyl nitrates in the chemical mechanism, NO<sub>2</sub> will increase by roughly 3% in urban areas and 18% in rural areas. Second, an underestimate in VOC emissions would have an impact on peroxyacyl and alkyl nitrate formation, and should enhance the effective NO<sub>x</sub> lifetime (Romer et al., 2016). Third, the temporal allocation of bottom-up emissions inventories can be a very significant source of uncertainty (Mues et al., 2014). The temporal allocation of the bottom-up Korean NO<sub>x</sub> emissions in this WRF-Chem simulation is such that the early afternoon rate during the OMI overpass time (between 12:00 – 14:00 local time) is approximately equal to 24-hour averaged rate (Figure 4). For comparison, using SMOKE in the eastern US yields an, the early afternoon emission rate that is 1.35 larger than the 24-hour averaged emission rate. Thus, there are scenarios in which the temporal allocation can be up to 35% different in the mid-afternoon during the OMI overpass time. We are not suggesting that the Korean emissions inventory should have the diurnal profile of the US or vice versa, but instead that there are scenarios in which the temporal allocation can vary widely. This substantiates the future use of geostationary satellites to better constrain this temporal allocation uncertainty. Lastly, the remaining difference will likely be due to an underestimate in the emissions inventory.

### 3.4 Comparing WRF-Chem to Aircraft Measurements

When comparing the model simulation to in situ observations from the UC-Berkeley NO<sub>2</sub> instrument aboard the aircraft, we find that NO<sub>2</sub> concentrations are substantially larger than the model when spatially and temporally collocated in the immediate Seoul metropolitan area (Figure 5). The comparison isolates the NO<sub>2</sub> within the lowermost boundary layer as the primary contributor to the tropospheric column underestimate. When comparing aircraft NO<sub>2</sub> to modeled NO<sub>2</sub> in other areas of the Korean peninsula, the underestimate is smaller.

When comparing the model simulation of NO<sub>y</sub> to observations of the same quantity observed from the aircraft, we find a similarly large underestimate. NO<sub>y</sub> observed on the aircraft is roughly a factor of two larger at all altitudes below 2 km. This suggests that errors in NO<sub>2</sub> recycling (NO<sub>2</sub> ↔ NO<sub>y</sub>) are not the main cause of the NO<sub>2</sub> discrepancies seen in the satellite and aircraft comparison (also see Figure 9). Instead, there must be errors in the NO<sub>y</sub> production (i.e., NO<sub>x</sub> emission rates are too low) or removal rates (i.e., NO<sub>y</sub> deposition rates are too slow).

### 3.5 Comparison of OMI NO<sub>2</sub> to Pandora NO<sub>2</sub>

To quantify the skill of the regional OMI NO<sub>2</sub> product, we compare the new total NO<sub>2</sub> vertical columns from the satellite product to the same quantities observed by the Pandora instruments. In Figure 6, monthly averaged observations during May 2016 from the Pandora instrument are overlaid onto the monthly average of the three OMI NO<sub>2</sub> satellite products. The two regional OMI NO<sub>2</sub> products capture the magnitude and spatial variability of monthly averaged NO<sub>2</sub> within the metropolitan region better.

We then compare daily Pandora observations to each daily OMI NO<sub>2</sub> value spatially and temporally collocated with the Pandora instrument (Figure 6). The Pandora observation is a 2-hour mean centered on the mid-afternoon OMI overpass. The slope of the linear best-fit of the standard product is 0.58, indicating that there is a consistent low bias in the satellite product when the Pandora instrument observes large values. [A similar result was also found by Herman et al. \(2018\).](#) The best-fit slope of the OMI-Regional product with only the air mass factor adjustment (AMF) is 0.76, and the OMI-Regional product with the air mass factor adjustment and spatial kernel (AMF+SK) is 1.07, indicating that the regional products capture the polluted-to-clean spatial gradients best. The correlation of daily observations to the satellite retrievals does not improve between retrievals (OMI-Standard:  $r^2 = 0.57$ , OMI-Regional (AMF):  $r^2 = 0.57$ , and OMI-Regional (AMF+SK):  $r^2 = 0.58$ ). The lack of improvement in the correlation suggests that the forecasted WRF-Chem simulation is unable to capture the daily variability of NO<sub>2</sub> plumes better than a longer-term average.

### 3.6 Estimating NO<sub>x</sub> emissions from Seoul

To estimate NO<sub>x</sub> emissions from the Seoul metropolitan area using a top-down satellite-based approach, we follow the exponentially modified Gaussian (EMG) fitting methodology outlined in Section 2.5. When fit using the EMG method, the photochemical lifetime and OMI NO<sub>2</sub> burden can be derived. Using this information, a NO<sub>x</sub> emission rate can be inferred.

#### 3.6.1. Validating the EMG method using WRF-Chem

The WRF-Chem simulation can serve as a test bed to assess the accuracy of the EMG method, since the bottom-up emissions used for the simulation are known. For this study, we find that for Seoul, an across plume width of 160 km encompasses the entire NO<sub>2</sub> downwind plume. Using the NO<sub>2</sub> lifetime, NO<sub>2</sub> burden, and a 160 km across plume width, we calculate the top-down NO<sub>x</sub> emissions rate in the WRF-Chem simulation from the Seoul metropolitan area during the early afternoon (Figure 7). We find the effective NO<sub>2</sub> photochemical lifetime to be  $3.1 \pm 1.3$  hours and the emissions rate to be  $227 \pm 94$  kton/yr NO<sub>2</sub> equivalent. Uncertainties of the top-down NO<sub>x</sub> emissions are the square root of the sum of the squares of: the NO<sub>x</sub> / NO<sub>2</sub> ratio (10%), the OMI NO<sub>2</sub> vertical columns (25%), the across plume width (10%), and the wind fields (30%) (Lu et al., 2015). Only the latter three terms are used to calculate the uncertainty of the NO<sub>2</sub> lifetime (Lu et al., 2015).

The NO<sub>x</sub> bottom-up emissions inventory calculated using a 40 km radius from the Seoul city center is 198 kton/yr NO<sub>2</sub> equivalent. We use a 40 km radius in lieu of a larger radius because an assumption in EMG method is that the



emissions must be clustered around a single point (in this case, the city center). Therefore, the calculated emissions rate from the EMG fit is only measuring the magnitude of the perturbing emission source, and not of smaller sources that are further from the city center. Previous studies (de Foy et al., 2014; de Foy et al., 2015) suggest that the background level calculated by the EMG fit accounts for emissions outside the plume that are more regional and diffuse in nature. The agreement between the top-down (227 kton/yr) and bottom-up (198 kton/yr) approaches demonstrates the accuracy and effectiveness of the EMG method in estimating the emissions rate.

### 3.6.2. Deriving emissions using OMI NO<sub>2</sub>

We now calculate the top-down NO<sub>x</sub> emissions rate from the satellite data from the Seoul metropolitan area during the early afternoon (Figure 8). Here we use the OMI standard product and the OMI NO<sub>2</sub> retrieval without the spatial averaging kernel; only the new air mass factor is applied to this retrieval. We do not use the retrieval with the spatial averaging kernel when calculating top-down NO<sub>x</sub> emissions because the spatial averaging is strongly dependent on the wind fields in the WRF-Chem simulation, which are forecasted. Errors in the winds can greatly affect the estimate using this top-down approach (Valin et al., 2013; de Foy et al., 2014).

For the standard product, the effective NO<sub>2</sub> photochemical lifetime is  $4.2 \pm 1.7$  hours, while in the regional product, the effective lifetime is  $3.4 \pm 1.4$  hours. In the standard product, we derive the NO<sub>x</sub> emissions rate to be  $353 \pm 146$  kton/yr NO<sub>2</sub> equivalent, while in the regional product it is  $484 \pm 201$  kton/yr NO<sub>2</sub> equivalent. Emission estimates using satellite products with coarse resolution air mass factors will yield top-down emission estimates that are lower than reality. In this case, the regional satellite product yields NO<sub>x</sub> emission rates that are 37% higher; we would expect similar results from other metropolitan regions. The top-down approach for the model simulation yielded a NO<sub>x</sub> emission rate of 227 kton/yr, while the top-down approach using the satellite data yielded a 484 kton/yr NO<sub>x</sub> emission rate: a 53% underestimate in the emissions inventory.

It should be noted that the NO<sub>2</sub> photochemical lifetime derived here is a fundamentally different quantity than the NO<sub>2</sub> lifetime observed by in situ measurements (de Foy et al., 2014; Lu et al., 2015) or derived by model simulations (Lamsal et al., 2010). This is because the lifetime calculation is extremely sensitive to the accuracy of the wind direction (de Foy et al., 2014) and spatial pattern of the emissions. Inaccuracies in the wind fields introduce noise that shorten the tail of the fit. As a result, NO<sub>2</sub> photochemical lifetimes derived here are considered “effective” photochemical lifetimes and are universally-generally shorter than the tropospheric column NO<sub>2</sub> lifetimes derived by model simulations (Lamsal et al., 2010). NO<sub>x</sub> sources at the outer portions of urban areas will lead to an artificially longer NO<sub>2</sub> lifetime. This partially compensates for the bias introduced by the wind direction. The heterogeneous topography and oscillating thermally driven wind flows (such as the Yellow Sea breeze) in the Seoul metropolitan area are effects that may bias the effective photochemical lifetime calculation. We partially account for this bias by only selecting days with strong winds (>3 m/s); on days with faster winds speeds, the sea & mountain breeze effects are secondary to the synoptic flow. The effective photochemical lifetime is also different from the NO<sub>2</sub> lifetime derived by in situ measurements of NO<sub>2</sub> at the surface or within the boundary layer. In the boundary layer, NO<sub>2</sub> is

~~consumed faster yielding lifetimes that are shorter than the lifetimes based on tropospheric columns (Nunnermacker et al., 2007).~~

### 3.7. Model simulation with increased NO<sub>x</sub> emissions

To test whether an increase in the NO<sub>x</sub> emission rate is appropriate for the Seoul metropolitan area, we conduct a simulation with NO<sub>x</sub> emissions in the Seoul metropolitan area – within a 40 km radius of the city center – increased by a factor of 2.13, and analyze the results for May 2016. The 2.13 increase is representative of the change suggested by the top-down method (OMI-Regional: 484 kton/yr vs. WRF-Chem original: 227 kton/yr). This simulation was performed slightly differently than the original simulation in that it was a continuous month-long simulation and the outer domain was nudged to the reanalysis.

When comparing the new model simulation to in situ observations from the UC-Berkeley NO<sub>2</sub> and NCAR NO<sub>y</sub> instruments aboard the DC-8 aircraft, we find that NO<sub>2</sub> concentrations are a bit high, but NO<sub>y</sub> concentrations are in good agreement with WRF-Chem in the boundary layer when spatially and temporally collocated in the immediate Seoul metropolitan area (Figure 9). The NO<sub>2</sub>-NO<sub>y</sub> partitioning is captured well by both model simulations, and there is no significant change in the NO<sub>2</sub>-NO<sub>y</sub> ratio when using increased NO<sub>x</sub> emissions.

When comparing the new WRF-Chem simulation to the OMI-Regional product for May 2016 (Figure 10), we now find no significant biases in the Seoul metropolitan area. In the area within 40 km of the Seoul city center, NO<sub>2</sub> columns are now only 11% smaller in the new model simulation. The better agreement in NO<sub>2</sub> and NO<sub>y</sub> from a combination of aircraft and satellite data suggests that an increase in NO<sub>x</sub> emissions by a factor of 2.13 is appropriate.

Finally, we re-process the air mass factors for May 2016 using the newest WRF-Chem simulation. In Figure 11, we show the OMI-Standard product, the OMI-Regional product with no scaling of the a priori profiles from the original WRF-Chem simulation, the OMI-Regional product with scaling of the original a priori profiles, and the OMI-Regional product with a priori profiles from the new WRF-Chem simulation. While using the new a priori profiles increases the OMI NO<sub>2</sub> retrieval further by 8%, this change is much smaller than the 37% increase associated with switching models and model resolution (i.e., Standard vs. Regional product).

## 4. Conclusions and Discussion

In this work, we use a high-resolution (4 × 4 km<sup>2</sup>) WRF-Chem model simulation to re-calculate satellite NO<sub>2</sub> air mass factors over South Korea. We also apply a spatial averaging kernel to better account for the sub-pixel variability that cannot be observed by OMI. The regional OMI NO<sub>2</sub> retrieval yields increased tropospheric columns in city centers and near large industrial areas. In the area within 40 km of the Seoul city center, OMI NO<sub>2</sub> values are 1.37 larger in the regional product. Areas near large industrial sources have OMI NO<sub>2</sub> values that are >2 times larger. The increase in remotely sensed tropospheric vertical column contents in the Seoul metropolitan area is in better agreement with the Pandora NO<sub>2</sub> spectrometer measurements acquired during the KORUS-AQ field campaign.

Using the regional OMI NO<sub>2</sub> product with only the air mass factor correction applied, we derive the NO<sub>x</sub> emissions rate from the Seoul metropolitan area to be 484 ± 201 kton/yr, while the standard NASA OMI NO<sub>2</sub> product gives an emissions rate of 353 ± 146 kton/yr. The WRF-Chem simulation yields a mid-afternoon NO<sub>x</sub> emission rate of 227 ± 94 kton/yr. This suggests an underestimate in the bottom-up NO<sub>x</sub> emissions from Seoul metropolitan area by 53%,  
5 when compared to the 484 kton/yr emissions rate from our top-down method. When comparing observed OMI NO<sub>2</sub> to the WRF-Chem model simulation, we find similar underestimates of NO<sub>2</sub> in the Seoul metropolitan area. The effective photochemical lifetime derived in the Seoul plume is 4.2 ± 1.7 hours using the standard OMI NO<sub>2</sub> product and 3.4 ± 1.4 hours using the regional product. The regional product yields shorter NO<sub>2</sub> lifetimes, although it is not a statistically significant difference. Finally, we show that a WRF-Chem simulation with an increase in the NO<sub>x</sub>  
10 emissions by a factor of 2.13 yields a better comparison with aircraft observations of NO<sub>2</sub> and NO<sub>y</sub>, and is in better agreement with the OMI-Regional NO<sub>2</sub> product developed herein.

It should be noted that the Seoul metropolitan area has complex geographical features, which adds further uncertainty to this analysis. The area has large topographical changes over short distances, including many hills (> 500 m) within the metropolitan area. Furthermore, the city is in close proximity to the Yellow Sea, which causes the area to be  
15 affected by sea breeze fronts, especially in the springtime, which is our period of focus. The localized mountain and sea breezes may not be fully captured by our 4 × 4 km<sup>2</sup> WRF-Chem simulation used to derive the OMI-Regional product or the ERA-interim dataset used to calculate top-down NO<sub>x</sub> emissions. The effects of these features on local air quality have been documented elsewhere in the literature (Kim and Ghim, 2002; Lee et al., 2008; Ryu et al., 2013).  
20 ~~We do not expect any consistent bias to result from this added uncertainty.~~ Nevertheless, the 4 × 4 km<sup>2</sup> simulation will capture topography and mesoscale phenomena better than a coarse global model and further supports the benefits of WRF-Chem over a global model to derive NO<sub>2</sub> vertical column contents.

We hypothesize that the ~~temporalization-temporal allocation~~ of NO<sub>x</sub> emissions in the bottom-up emission inventory is a large remaining uncertainty. The satellite-derived emission rates are instantaneous rates at the time of the OMI overpass (~13:45 local time). This is a different quantity than a bottom-up NO<sub>x</sub> emission inventory, which is often a  
25 daily averaged or monthly averaged emission rate. For this study, we only attempt to derive a mid-afternoon NO<sub>x</sub> emission rate. Subsequently, we make sure to compare this to the mid-afternoon NO<sub>x-\*</sub> emission rate from WRF-Chem. While bottom-up studies provide estimates of the diurnal variability of NO<sub>x</sub> emissions, these are very difficult to confirm from top-down approaches. Due to a consistent mid-afternoon overpass time, OMI or TROPOMI cannot address this issue. Due to boundary layer dynamics, this is also very difficult to constrain from ground-based and  
30 aircraft measurements. In the future, observations from a geostationary satellite instruments such as the Geostationary Environment Monitoring Spectrometer (GEMS) and Tropospheric Emissions: Monitoring Pollution (TEMPO), will be ~~helpful-integral~~ in constraining the ratio of the mid-afternoon emissions rate to the 24-hour averaged emission rate.

## Acknowledgments

This publication was developed using funding from the NASA KORUS-AQ science team and the NASA Atmospheric Composition Modeling and Analysis Program (ACMAP). We would like to thank the NASA Pandora Project Team, including Jay Herman and Bob Swap of NASA Goddard Space Flight Center, Jim Szykman of EPA, and the ESA-Pandonia team from Luftblick in supporting the deployment and maintenance of the Pandora instruments as well as the acquisition and processing of those observations during KORUS-AQ. We would also like to thank Ron Cohen of UC-Berkeley and his research group for their observations of NO<sub>2</sub> from the DC-8 aircraft during this same time period, and Andy Weinheimer of NCAR and his research group for their observations of NO<sub>y</sub> from the DC-8 aircraft. We would also like to thank Louisa Emmons and Gaby Pfister for their support in running the WRF-Chem simulation.

10 Additionally, we would like to thank Jim Crawford of NASA Langley and Barry Lefer of NASA Headquarters for their input on this research article. All data from KORUS-AQ can be downloaded freely from <http://www-air.larc.nasa.gov/cgi-bin/ArcView/discover-aq.dc-2011>. We acknowledge the free use of NO<sub>2</sub> column data from the OMI sensor available at: [https://disc.gsfc.nasa.gov/Aura/data-holdings/OMI/omno2\\_v003.shtml](https://disc.gsfc.nasa.gov/Aura/data-holdings/OMI/omno2_v003.shtml). The submitted manuscript has been created by UChicago Argonne, LLC, Operator of Argonne National Laboratory (“Argonne”).

15 Argonne, a U.S. Department of Energy Office of Science laboratory, is operated under Contract No. DE-AC02-06CH11357. The U.S. Government retains for itself, and others acting on its behalf, a paid-up nonexclusive, irrevocable worldwide license in said article to reproduce, prepare derivative works, distribute copies to the public, and perform publicly and display publicly, by or on behalf of the Government.

## References

- Allen, D. J., Pickering, K. E., Pinder, R. W., Henderson, B. H., Appel, K. W., and Prados, A.: Impact of lightning-NO on eastern United States photochemistry during the summer of 2006 as determined using the CMAQ model, *Atmos. Chem. Phys.*, 12, 1737-1758, 2012.
- 5 Beirle, S., Boersma, K. F., Platt, U., Lawrence, M. G., and Wagner, T.: Megacity Emissions and Lifetimes of Nitrogen Oxides Probed from Space, *Science*, 333, 1737-1739, 2011.
- Boersma, K. F., Jacob, D. J., Bucsela, E. J., Perring, A. E., Dirksen, R., Yantosca, R. M., Park, R. J., Wenig, M. O., Bertram, T. H., and Cohen, R. C.: Validation of OMI tropospheric NO<sub>2</sub> observations during INTEX-B and application to constrain NO<sub>x</sub> emissions over the eastern United States and Mexico, *Atmos. Environ.*, 42, 4480-4497, 2008.
- 10 Boersma, K. F., Eskes, H. J., Dirksen, R. J., Veefkind, J. P., Stammes, P., Huijnen, V., Kleipool, Q. L., Sneep, M., Claas, J., and Leitão, J.: An improved tropospheric NO<sub>2</sub> column retrieval algorithm for the Ozone Monitoring Instrument, *Atmos. Meas. Tech.*, 4, 1905, 2011.
- Boersma, K. F., Vinken, G. C. M., and Tournadre, J.: Ships going slow in reducing their NO<sub>x</sub> emissions: changes in 2005–2012 ship exhaust inferred from satellite measurements over Europe, *Environ. Res. Lett.*, 10, 074007, 2015.
- 15 Bucsela, E., Krotkov, N., Celarier, E., Lamsal, L., Swartz, W., Bhartia, P., Boersma, K., Veefkind, J., Gleason, J., and Pickering, K.: A new algorithm for retrieving vertical column NO<sub>2</sub> from nadir-viewing satellite instruments: applications to OMI, *Atmos. Meas. Tech.*, 6, 1361-1407, 2013.
- Burrows, J. P., Weber, M., Buchwitz, M., Rozanov, V., Ladstätter-Weissenmayer, A., Richter, A., DeBeek, R., Hoogen, R., Bramstedt, K., Eichmann, K.-U., Eisinger, M., and Perner, D.: The Global Ozone Monitoring Experiment (GOME): Mission Concept and First Scientific Results, *J. Atmos. Sci.*, 56, 151–175, 1999.
- 20 Canty, T. P., Hembeck, L., Vinciguerra, T. P., Anderson, D. C., Goldberg, D. L., Carpenter, S. F., Allen, D. J., Loughner, C. P., Salawitch, R. J., and Dickerson, R. R.: Ozone and NO<sub>x</sub> chemistry in the eastern US: evaluation of CMAQ/CB05 with satellite (OMI) data, *Atmos. Chem. Phys.*, 15, 10965-10982, 2015.
- 25 Chen, D., Zhou, B., Beirle, S., Chen, L. M., and Wagner, T.: Tropospheric NO<sub>2</sub> column densities deduced from zenith-sky DOAS measurements in Shanghai, China, and their application to satellite validation, *Atmos. Chem. Phys.*, 9, 3641-3662, 2009.
- [Chong, H., Lee, H., Koo, J.-H., Kim, J., Jeong, U., Kim, W., Kim, S.-W., Herman, J., Abuhassan, N. K., Ahn, J.-Y., Park, J.-H., Kim, S.-K., Moon, K.-J., Choi, W.-J., Park, S. S.: Regional Characteristics of NO<sub>2</sub> Column Densities from Pandora Observations during the MAPS-Seoul Campaign. \*Aerosol and Air Quality Research\*, 18, 2207-2219, 2018.](#)
- 30 Curier, R. L., Kranenburg, R., Segers, A. J. S., Timmermans, R. M. A., and Schaap, M.: Synergistic use of OMI NO<sub>2</sub> tropospheric columns and LOTOS-EUROS to evaluate the NO<sub>x</sub> emission trends across Europe, *Remote Sensing of Environment*, 149, 58-69, 2014.
- 35 Day, D. A., Wooldridge, P. J., Dillon, M. B., Thornton, J. A., and Cohen, R. C.: A thermal dissociation laser-induced fluorescence instrument for in situ detection of NO<sub>2</sub>, peroxy nitrates, alkyl nitrates, and HNO<sub>3</sub>, *J. Geophys. Res. Atmos.*, 107, ARTN 4046, 2002.
- Dee, D. P., Uppala, S. M., Simmons, A. J., Berrisford, P., Poli, P., Kobayashi, S., Andrae, U., Balmaseda, M. A., Balsamo, G., Bauer, P., Bechtold, P., Beljaars, A. C. M., van de Berg, L., Bidlot, J., Bormann, N., Delsol, C., Dragani, R., Fuentes, M., Geer, A. J., Haimberger, L., Healy, S. B., Hersbach, H., Hólm, E. V., Isaksen, I., Kållberg, P., Köhler, M., Matricardi, M., McNally, A. P., Monge-Sanz, B. M., Morcrette, J.-J., Park, B.-K., Peubey, C., de Rosnay, P., Tavolato, C., Thépaut, J.-N., and Vitart, F.: The ERA-Interim reanalysis: configuration and performance of the data assimilation system, *Q. J. Roy. Meteorol. Soc.*, 137, 553–597, doi:10.1002/qj.828, 2011.
- 40 de Foy, B., Lu, Z., and Streets, D. G.: Satellite NO<sub>2</sub> retrievals suggest China has exceeded its NO<sub>x</sub> reduction goals from the twelfth Five-Year Plan, *Scientific Reports*, 6, 2016.
- de Foy, B., Lu, Z., Streets, D. G., Lamsal, L. N., and Duncan, B. N.: Estimates of power plant NO<sub>x</sub> emissions and lifetimes from OMI NO<sub>2</sub> satellite retrievals, *Atmos. Environ.*, 116, 1-11, 2015.
- 45 de Foy, B., Wilkins, J. L., Lu, Z., Streets, D. G., Duncan, B. N.: Model evaluation of methods for estimating surface emissions and chemical lifetimes from satellite data. *Atmos. Environ.* 98, 66-77, 2014.
- 50 Dobber, M., Kleipool, Q., Dirksen, E., Levelt, P., Jaross, G., Taylor, S., Kelly, T., Flynn, L., Leppelmeier, G., and Rozemeijer, N.: Validation of Ozone Monitoring Instrument level 1b data products, *J. Geophys. Res. Atmos.*, 113, D15S06, 2008.
- Duncan, B. N., Lamsal, L. N., Thompson, A. M., Yoshida, Y., Lu, Z., Streets, D. G., Hurwitz, M. M., and Pickering,

- K. E.: A space based, high resolution view of notable changes in urban NO<sub>x</sub> pollution around the world (2005–2014), *J. Geophys. Res. Atmos.*, 121, 976-996, 2016.
- 5 Flynn, C. M., Pickering, K. E., Crawford, J. H., Lamsal, L., Krotkov, N., Herman, J., Weinheimer, A., Chen, G., Liu, X., and Szykman, J.: Relationship between column-density and surface mixing ratio: Statistical analysis of O<sub>3</sub> and NO<sub>2</sub> data from the July 2011 Maryland DISCOVER-AQ mission, *Atmos. Environ.*, 92, 429-441, 2014.
- 10 Goldberg, D. L., Lamsal, L. N., Loughner, C. P., Swartz, W. H., Lu, Z., and Streets, D. G.: A high-resolution and observationally constrained OMI NO<sub>2</sub> satellite retrieval, *Atmos. Chem. Phys.*, 17, 11403-11421, <https://doi.org/10.5194/acp-17-11403-2017>, 2017.
- 15 Goldberg, D. L., Vinciguerra, T. P., Anderson, D. C., Hembeck, L., Canty, T. P., Ehrman, S. H., Martins, D. K., Stauffer, R. M., Thompson, A. M., Salawitch, R. J., and Dickerson R. R.: CAMx ozone source attribution in the eastern United States using guidance from observations during DISCOVER-AQ Maryland, *Geophys. Res. Lett.*, 43, <https://dx.doi.org/10.1002/2015GL067332>, 2016.
- 20 Grell, G., Peckham, S. E., Schmitz, R., McKeen, S. A., Frost, G., Skamarock, W. C., and Eder, B.: Fully coupled “online” chemistry within the WRF model, *Atmospheric Environment*, 39, 6957-6975, [10.1016/j.atmosenv.2005.04.027](https://doi.org/10.1016/j.atmosenv.2005.04.027), 2005.
- 25 Han, K. M., Lee, S., Chang, L. S., and Song, C. H.: A comparison study between CMAQ-simulated and OMI-retrieved NO<sub>2</sub> columns over East Asia for evaluation of NO<sub>x</sub> emission fluxes of INTEX-B, CAPSS, and REAS inventories, *Atmos. Chem. Phys.*, 15, 1913-1938, 2015.
- 30 Herman, J., Cede, A., Spinei, E., Mount, G., Tzortziou, M., and Abuhassan, N.: NO<sub>2</sub> column amounts from ground-based Pandora and MFDOAS spectrometers using the direct-sun DOAS technique: Intercomparisons and application to OMI validation, *J. Geophys. Res.*, 114, D13307, 2009.
- 35 Herman, J., Spinei, E., Fried, A., Kim, J., Kim, J., Kim, W., Cede, A., Abuhassan, N., and Segal-Rozenhaimer, M.: NO<sub>2</sub> and HCHO measurements in Korea from 2012 to 2016 from Pandora spectrometer instruments compared with OMI retrievals and with aircraft measurements during the KORUS-AQ campaign, *Atmos. Meas. Tech.*, 11, 4583-4603, <https://doi.org/10.5194/amt-11-4583-2018>, 2018
- 40 Hilboll, A., Richter, A., and Burrows, J. P.: Long-term changes of tropospheric NO<sub>2</sub> over megacities derived from multiple satellite instruments, *Atmos. Chem. Phys.*, 13, 4145-4169, 2013.
- 45 Hodzic, A., and Jimenez, J. L.: Modeling anthropogenically controlled secondary organic aerosols in a megacity: a simplified framework for global and climate models, *Geosci. Model Dev.*, 4, 901-917, [10.5194/gmd-4-901-2011](https://doi.org/10.5194/gmd-4-901-2011), 2011.
- 50 Hudman, R. C., Russell, A. R., Valin, L. C., and Cohen, R. C.: Interannual variability in soil nitric oxide emissions over the United States as viewed from space, *Atmos. Chem. Phys.*, 10, 9943-9952, 2010.
- 55 Huijnen, V., Eskes, H. J., Poupkou, A., Elbern, H., Boersma, K. F., Foret, G., Sofiev, M., Valdebenito, A., Flemming, J., Stein, O., Gross, A., Robertson, L., D'Isidoro, M., Kioutsioukis, I., Friese, E., Amstrup, B., Bergstrom, R., Strunk, A., Vira, J., Zyryanov, D., Maurizi, A., Melas, D., Peuch, V.-H., and Zerefos, C.: Comparison of OMI NO<sub>2</sub> tropospheric columns with an ensemble of global and European regional air quality models, *Atmos. Chem. Phys.*, 10, 3273-3296, [doi:10.5194/acp-10-3273-2010](https://doi.org/10.5194/acp-10-3273-2010), 2010.
- 60 Ialongo, I., Herman, J., Krotkov, N., Lamsal, L., Boersma, K. F., Hovila, J., and Tamminen, J.: Comparison of OMI NO<sub>2</sub> observations and their seasonal and weekly cycles with ground-based measurements in Helsinki, *Atmos. Meas. Tech.*, 9, 5203, 2016.
- 65 Inness, A., Blechschmidt, A. M., Bouarar, I., Chabrillat, S., Crepulja, M., Engelen, R. J., Eskes, H., Flemming, J., Gaudel, A., Hendrick, F., Huijnen, V., Jones, L., Kapsomenakis, J., Katragkou, E., Keppens, A., Langerock, B., de Mazière, M., Melas, D., Parrington, M., Peuch, V. H., Razinger, M., Richter, A., Schultz, M. G., Suttie, M., Thouret, V., Vrekoussis, M., Wagner, A., and Zerefos, C.: Data assimilation of satellite retrieved ozone, carbon monoxide and nitrogen dioxide with ECMWF's Composition-IFS, *Atmos. Chem. Phys. Discuss.*, 15, 4265-4331, [10.5194/acpd-15-4265-2015](https://doi.org/10.5194/acpd-15-4265-2015), 2015.
- 70 Kim, H. C., Lee, P., Judd, L., Pan, L., and Lefer, B.: OMI NO<sub>2</sub> column densities over North American urban cities: the effect of satellite footprint resolution, *Geosci. Mod. Dev.*, 9, 1111-1123, 2016.
- 75 Kim, J. Y., and Ghim, Y. S.: Effects of the density of meteorological observations on the diagnostic wind fields and performance of photochemical modeling in the great Seoul area, *Atmos. Environ.*, 36, 201-212, 2002.
- 80 Kleipool, Q. L., Dobber, M. R., de Haan, J. F., and Levelt, P. F.: Earth surface reflectance climatology from 3 years of OMI data, *J. Geophys. Res. Atmos.*, 113, 2008.
- 85 Krotkov, N. A., McLinden, C. A., Li, C., Lamsal, L. N., Celarier, E. A., Marchenko, S. V., Swartz, W. H., Bucsela, E. J., Joiner, J., and Duncan, B. N.: Aura OMI observations of regional SO<sub>2</sub> and NO<sub>2</sub> pollution changes from 2005 to 2014, *Atmos. Chem. Phys.*, 16, 4605-4629, 2016.
- 90 Krotkov, N. A., Lamsal, L. N., Celarier, E. A., Swartz, W. H., Marchenko, S. V., Bucsela, E. J., Chan, K. L., and

- Wenig, M. O.: The version 3 OMI NO<sub>2</sub> standard product, *Atmos. Meas. Tech. Discuss.*, in review, 2017.
- Kuhlmann, G., Lam, Y. F., Cheung, H. M., Hartl, A., Fung, J. C. H., Chan, P. W., and Wenig, W. O.: Development of a custom OMI NO<sub>2</sub> data product for evaluating biases in a regional chemistry transport model, *Atmos. Chem. Phys.*, 15, 5627-5644, 2015.
- 5 Lamsal, L. N., Martin, R. V., van Donkelaar, A., Steinbacher, M., Celarier, E. A., Bucsela, E., Dunlea, E. J., and Pinto, J. P.: Ground-level nitrogen dioxide concentrations inferred from the satellite-borne Ozone Monitoring Instrument, *J. Geophys. Res.*, 113, D16308, 2008.
- Lamsal, L. N., Martin, R. V., van Donkelaar, A., Celarier, E. A., Bucsela, E. J., Boersma, K. F., Dirksen, R., Luo, C., and Wang, Y.: Indirect validation of tropospheric nitrogen dioxide retrieved from the OMI satellite instrument: Insight into the seasonal variation of nitrogen oxides at northern midlatitudes, *J. Geophys. Res.*, 115, D05302, doi:10.1029/2009jd013351, 2010.
- 10 Lamsal, L. N., Krotkov, N. A., Celarier, E. A., Swartz, W. H., Pickering, K. E., Bucsela, E. J., Gleason, J. F., Martin, R. V., Philip, S., and Irie, H.: Evaluation of OMI operational standard NO<sub>2</sub> column retrievals using in situ and surface-based NO<sub>2</sub> observations, *Atmos. Chem. Phys.*, 14, 11587-11609, 2014.
- 15 Lamsal, L. N., Duncan, B. N., Yoshida, Y., Krotkov, N. A., Pickering, K. E., Streets, D. G., and Lu, Z.: US NO<sub>2</sub> trends (2005 - 2013): EPA Air Quality System (AQS) data versus improved observations from the Ozone Monitoring Instrument (OMI), *Atmos. Environ.*, 110, 130-143, 2015.
- Laughner, J. L., Zare, A., and Cohen, R. C.: Effects of daily meteorology on the interpretation of space-based remote sensing of NO<sub>2</sub>, *Atmos. Chem. Phys.*, 16, 15247-15264, 2016.
- 20 Laughner, J. L., Zhu, Q., and Cohen, R. C.: Evaluation of version 3.0B of the BEHR OMI NO<sub>2</sub> product, *Atmos. Meas. Tech.*, 12, 129-146, <https://doi.org/10.5194/amt-12-129-2019>, 2019.
- Lee, H. W., Choi, H.-J., Lee, S.-H., Kim, Y.-K., Jung, W.-S.: The impact of topography and urban building parameterization on the photochemical ozone concentration of Seoul, Korea, *Atmos. Environ.*, 42(18), 4232-4246, 2008.
- 25 Levelt, P. F., Van den Oord, G. H. J., Dobber, M. R., Malkki, A., Visser, H., de Vries, J., Stammes, P., Lundell, J. O. V., and Saari, H.: The Ozone Monitoring Instrument, *IEEE Trans. Geosci. Rem. Sens.*, 44, 1093-1101, 2006.
- Liaskos, C. E., Allen, D. J., and Pickering, K. E.: Sensitivity of tropical tropospheric composition to lightning NO<sub>x</sub> production as determined by replay simulations with GEOS-5, *J. Geophys. Res. Atmos.*, 2015.
- 30 Lin, J. T., Liu, M. Y., Xin, J. Y., Boersma, K. F., Spurr, R., Martin, R., and Zhang, Q.: Influence of aerosols and surface reflectance on satellite NO<sub>2</sub> retrieval: seasonal and spatial characteristics and implications for NO<sub>x</sub> emission constraints, *Atmos. Chem. Phys.*, 15, 11217-11241, 2015.
- Liu, F., Beirle, S., Zhang, Q., Dörner, S., He, K., and Wagner, T.: NO<sub>x</sub> lifetimes and emissions of cities and power plants in polluted background estimated by satellite observations, *Atmos. Chem. Phys.*, 16, 5283-5298, <https://doi.org/10.5194/acp-16-5283-2016>, 2016.
- 35 Liu, F., Beirle, S., Zhang, Q., van der A, R. J., Zheng, B., Tong, D., and He, K.: NO<sub>x</sub> emission trends over Chinese cities estimated from OMI observations during 2005 to 2015, *Atmos. Chem. Phys.*, 17, 9261-9275, <https://doi.org/10.5194/acp-17-9261-2017>, 2017.
- Lorente, A., Boersma, K. F., Yu, H., Dörner, S., Hilboll, A., Richter, A., Liu, M., Lamsal, L. N., Barkley, M., and De Smedt, I.: Structural uncertainty in air mass factor calculation for NO<sub>2</sub> and HCHO satellite retrievals, *Atmos. Meas. Tech.*, 10, 759, 2017.
- 40 Lu, Z., Streets, D. G., de Foy, B., Lamsal, L. N., Duncan, B. N., and Xing, J.: Emissions of nitrogen oxides from US urban areas: estimation from Ozone Monitoring Instrument retrievals for 2005–2014, *Atmos. Chem. Phys.*, 15, 10367-10383, 2015.
- 45 Ma, J. Z., Beirle, S., Jin, J. L., Shaiganfar, R., Yan, P., and Wagner, T.: Tropospheric NO<sub>2</sub> vertical column densities over Beijing: results of the first three years of ground-based MAX-DOAS measurements (2008–2011) and satellite validation, *Atmos. Chem. Phys.*, 13, 1547-1567, 2013.
- Martin, R. V., Chance, K., Jacob, D. J., Kurosu, T. P., Spurr, R. J. D., Bucsela, E., Gleason, J. F., Palmer, P. I., Bey, I., and Fiore, A. M.: An improved retrieval of tropospheric nitrogen dioxide from GOME, *J. Geophys. Res. Atmos.*, 107, 2002.
- 50 Miyazaki, K., Eskes, H., Sudo, K., Boersma, K. F., Bowman, K., and Kanaya, Y.: Decadal changes in global surface NO<sub>x</sub> emissions from multi-constituent satellite data assimilation, *Atmos. Chem. Phys.*, 17, 807-837, <https://doi.org/10.5194/acp-17-807-2017>, 2017.
- Mues, A., Kuenen, J., Hendriks, C., Manders, A., Segers, A., Scholz, Y., Hueglin, C., Builtjes, P., and Schaap, M.: Sensitivity of air pollution simulations with LOTOS-EUROS to the temporal distribution of anthropogenic emissions, *Atmos. Chem. Phys.*, 14, 939-955, <https://doi.org/10.5194/acp-14-939-2014>, 2014.
- 55 Nault, B. A., Laughner, J. L., Wooldridge, P. J., Crounse, J. D., Dibb, J., Diskin, G., Peischl, J., Podolske, J. R.,

- Pollack, I. B., Ryerson, T. B., Scheuer, E., Wennberg, P. O., and Cohen, R. C.: Lightning NO<sub>x</sub> Emissions: Reconciling Measured and Modeled Estimates With Updated NO<sub>x</sub> Chemistry, *Geophys. Res. Lett.*, 44, 9479–9488, <https://doi.org/10.1002/2017GL074436>, 2017.
- 5 Palmer, P. I., Jacob, D. J., Chance, K. V., Martin, R. V., Spurr, R. J. D., Kurosu, T., Bey, I., Yantosca, R. M., Fiore, A., and Li, Q.: Air mass factor formulation for spectroscopic measurements from satellites: Application to formaldehyde retrievals from the Global Ozone Monitoring Experiment, *J. Geophys. Res.*, 106, 14539-14550, 2001.
- 10 Pfister, G. G., Walters, S., Lamarque, J. F., Fast, J., Barth, M. C., Wong, J., Done, J., Holland, G., and Bruyère, C. L.: Projections of future summertime ozone over the U.S, *Journal of Geophysical Research: Atmospheres*, 119, 5559-5582, [10.1002/2013jd020932](https://doi.org/10.1002/2013jd020932), 2014.
- Pickering, K. E., Bucselá, E., D, Ring, A., Holzworth, R., and Krotkov, N.: Estimates of lightning NO<sub>x</sub> production based on OMI NO<sub>2</sub> observations over the Gulf of Mexico, *J. Geophys. Res. Atmos.*, 121, 8668-8691, 2016.
- 15 Platt, U.: Differential optical absorption spectroscopy (DOAS), *Air monitoring by spectroscopic technique*, 127, 27-84, 1994.
- Pujadas, M., Núñez, L., and Lubrani, P.: Assessment of NO<sub>2</sub> satellite observations for en-route aircraft emissions detection, *Remote Sensing of Environment*, 115, 3298-3312, 2011.
- Rasool, Q. Z., Zhang, R., Lash, B., and Cohan, D. S., Cooter, E. J., Bash, J. O., Lamsal, L. N.: Enhanced representation of soil NO emissions in the Community Multiscale Air Quality (CMAQ) model version 5.0. 2, *Geosci. Mod. Dev.*, 9, 3177-3197, 2016.
- 20 Ridley, B., Ott, L., Pickering, K., Emmons, L., Montzka, D., Weinheimer, A., Knapp, D., Grahek, F., Li, L., Heymsfield, G., McGill, M., Kucera, P., Mahoney, M. J., Baumgarner, D., Schultz, M., and Brousseau, G.: Florida thunderstorms: A faucet of reactive nitrogen to the upper troposphere, *J. Geophys. Res. Atmos.*, 109, D17305, 2004.
- 25 Romer, P. S., Duffey, K. C., Wooldridge, P. J., Allen, H. M., Ayres, B. R., Brown, S. S., Brune, W. H., Crouse, J. D., de Gouw, J., Draper, D. C., Feiner, P. A., Fry, J. L., Goldstein, A. H., Koss, A., Misztal, P. K., Nguyen, T. B., Olson, K., Teng, A. P., Wennberg, P. O., Wild, R. J., Zhang, L., and Cohen, R. C.: The lifetime of nitrogen oxides in an isoprene-dominated forest, *Atmos. Chem. Phys.*, 16, 7623-7637, <https://doi.org/10.5194/acp-16-7623-2016>, 2016.
- 30 Russell, A. R., Valin, L. C., Bucselá, E. J., Wenig, M. O., and Cohen, R. C.: Space-based constraints on spatial and temporal patterns of NO<sub>x</sub> emissions in California, 2005-2008, *Environ. Sci. Technol.*, 44, 3608-3615, 2010.
- Russell, A. R., Perring, A. E., Valin, L. C., Bucselá, E. J., Browne, E. C., Wooldridge, P. J., and Cohen, R. C.: A high spatial resolution retrieval of NO<sub>2</sub> column densities from OMI: method and evaluation, *Atmos. Chem. Phys.*, 11, 8543-8554, 2011.
- 35 Ryu, Y.-H., Baik, J.-J., Kwak, K.-H., Kim, S., and Moon, N.: Impacts of urban land-surface forcing on ozone air quality in the Seoul metropolitan area, *Atmos. Chem. Phys.*, 13, 2177-2194, <https://doi.org/10.5194/acp-13-2177-2013>, 2013.
- 40 Saide, P. E., Carmichael, G. R., Liu, Z., Schwartz, C. S., Lin, H. C., da Silva, A. M., and Hyer, E.: Aerosol optical depth assimilation for a size-resolved sectional model: impacts of observationally constrained, multi-wavelength and fine mode retrievals on regional scale forecasts, *Atmos. Chem. Phys. Discuss.*, 13, 12213-12261, [10.5194/acpd-13-12213-2013](https://doi.org/10.5194/acpd-13-12213-2013), 2013.
- Saide, P. E., Kim, J., Song, C. H., Choi, M., Cheng, Y., and Carmichael, G. R.: Assimilation of next generation geostationary aerosol optical depth retrievals to improve air quality simulations, *Geophysical research letters*, 41, [2014GL062089](https://doi.org/10.1002/2014gl062089), [10.1002/2014gl062089](https://doi.org/10.1002/2014gl062089), 2014.
- 45 Skamarock, W. C., Klemp, J. B., Dudhia, J., Gill, D. O., Barker, D. M., Duda, M. G., Huang, X.-Y., Wang, W., and Powers, J. G.: A description of the Advanced Research WRF version 3, NCAR Tech. Note NCAR/TN-475+ STR, 2008.
- Souri, A. H., Choi, Y., Jeon, W., Li, X., Pan, S., Diao, L., and Westenbarger, D. A.: Constraining NO<sub>x</sub> emissions using satellite NO<sub>2</sub> measurements during 2013 DISCOVER-AQ Texas campaign, *Atmos. Environ.*, 131, 371-381, 2016.
- 50 Souri, A. H., Choi, Y., Jeon, W., Woo, J., Zhang, Q., and Kurokawa, J.: Remote sensing evidence of decadal changes in major tropospheric ozone precursors over East Asia *J. Geophys. Res. Atmos.*, 2017.
- Streets, D. G., Canty, T., Carmichael, G. R., de Foy, B., Dickerson, R. R., Duncan, B. N., Edwards, D. P., Haynes, J. A., Henze, D. K., Houyoux, M. R., Jacob, D. J., Krotkov, N. A., Lamsal, L. N., Liu, Y., Lu, Z., Martin, R. V., Pfister, G. G., Pinder R. W., Salawitch, R. J., Wecht, K. J.: Emissions estimation from satellite retrievals: A review of current capability, *Atmos. Environ.*, 77, 1011-1042, 2013.
- 55



- Thornton, J. A., Wooldridge, P. J., and Cohen R. C.: Atmospheric NO<sub>2</sub>: In situ laser-induced fluorescence detection at parts per trillion mixing ratios, *Analytical Chemistry*, 72, 528-539, 2000.
- Valin, L. C., Russell, A. R., and Cohen, R. C.: Variations of OH radicals in an urban plume inferred from NO<sub>2</sub> column measurements. *Geophys. Res. Lett.*, 40, 1856-1860, 2013.
- 5 van der A, R. J., Mijling, B., Ding, J., Koukouli, M. E., Liu, F., Li, Q., Mao, H., Theys, N.: Cleaning up the air: effectiveness of air quality policy for SO<sub>2</sub> and NO<sub>x</sub> emissions in China, *Atmos. Chem. Phys.*, 17, 1775–1789, 2017.
- van Vuuren, D. P., Bouwman, L. F., Smith, S. J., and Dentener, F.: Global projections for anthropogenic reactive nitrogen emissions to the atmosphere: an assessment of scenarios in the scientific literature, *Current Opinion in Environmental Sustainability*, 3, 359-369, 2011.
- 10 Vandaele, A. C., Hermans, C., Simon, P. C., Carleer, M., Colin, R., Fally, S., Merienne, M.-F., Jenouvrier, A., and Coquart, B.: Measurements of the NO<sub>2</sub> absorption cross-section from 42 000 cm<sup>-1</sup> to 10 000 cm<sup>-1</sup> (238–1000 nm) at 220 K and 294 K, *Journal of Quantitative Spectroscopy and Radiative Transfer*, 59, 171-184, 1998.
- Vasilkov, A., Qin, W., Krotkov, N., Lamsal, L., Spurr, R., Haffner, D., Joiner, J., Yang, E.-S., and Marchenko, S.: Accounting for the effects of surface BRDF on satellite cloud and trace-gas retrievals: a new approach based on geometry-dependent Lambertian equivalent reflectivity applied to OMI algorithms, *Atmos. Meas. Tech.*, 10, 333-349, <https://doi.org/10.5194/amt-10-333-2017>, 2017.
- Vinken, G. C. M., Boersma, K. F., Maasakkers, J. D., Adon, M., and Martin, R. V.: Worldwide biogenic soil NO<sub>x</sub> emissions inferred from OMI NO<sub>2</sub> observations, *Atmos. Chem. Phys.*, 14, 10363-10381, 2014a.
- 20 Vinken, G. C. M., Boersma, K. F., van Donkelaar, A., and Zhang, L.: Constraints on ship NO<sub>x</sub> emissions in Europe using GEOS-Chem and OMI satellite NO<sub>2</sub> observations, *Atmos. Chem. Phys.*, 14, 1353-1369, 2014b.
- Woo, J. H., Choi, K. C., Kim, H. K., Baek, B. H., Jang, M., Eum, J. H., Song, C. H., Ma, Y. I., Sunwoo, Y., Chang, L. S., and Yoo, S. H.: Development of an anthropogenic emissions processing system for Asia using SMOKE, *Atmos. Environ.*, 58, 5–13, 2012.
- 25 Zaveri, R. A., Easter, R. C., Fast, J. D., and Peters, L. K.: Model for simulating aerosol interactions and chemistry (MOSAIC), *J. Geophys. Res.*, 113, D13204, 2008.
- Zhang, L., Jacob, D. J., Boersma, K. F., Jaffe, D. A., Olson, J. R., Bowman, K. W., Worden, J. R., Thompson, A. M., Avery, M. A., Cohen, R. C., Dibb, J. E., Flock, F. M., Fuelberg, H. E., Huey, L. G., McMillan, W. W., Singh, H. B., and Weinheimer, A. J.: Transpacific transport of ozone pollution and the effect of recent Asian emission increases on air quality in North America: an integrated analysis using satellite, aircraft, ozonesonde, and surface observations, *Atmos. Chem. Phys.*, 8, 6117-6136, 2008.
- 30 Zheng, B., Tong, D., Li, M., Liu, F., Hong, C., Geng, G., Li, H., Li, X., Peng, L., Qi, J., Yan, L., Zhang, Y., Zhao, H., Zheng, Y., He, K., and Zhang, Q.: Trends in China's anthropogenic emissions since 2010 as the consequence of clean air actions, *Atmos. Chem. Phys.*, 18, 14095-14111, <https://doi.org/10.5194/acp-18-14095-2018>, 2018.
- 35 Zhou, Y., Brunner, D., Spurr, R. J. D., Boersma, K. F., Sneep, M., Popp, C., and Buchmann, B.: Accounting for surface reflectance anisotropy in satellite retrievals of tropospheric NO<sub>2</sub>, *Atmos. Meas. Tech.*, 3, 1185-1203, <https://doi.org/10.5194/amt-3-1185-2010>, 2010.
- Zhou, Y., Brunner, D., Boersma, K. F., Dirksen, R., and Wang, P.: An improved tropospheric NO<sub>2</sub> retrieval for OMI observations in the vicinity of mountainous terrain, *Atmos. Meas. Tech.*, 2, 401-416, <https://doi.org/10.5194/amt-2-401-2009>, 2009.
- 40

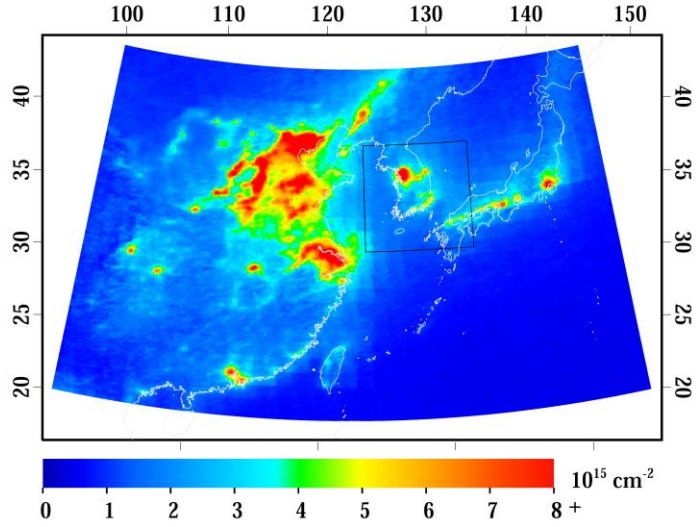


**Figure 1.** Warm season averaged (May – Sept)  $\text{NO}_2$  tropospheric vertical column content using the OMI-Standard  $\text{NO}_2$  product for the years of 2015 – 2017 in East Asia. The  $4 \times 4 \text{ km}^2$  WRF-Chem domain is outlined over the Korean peninsula.

5

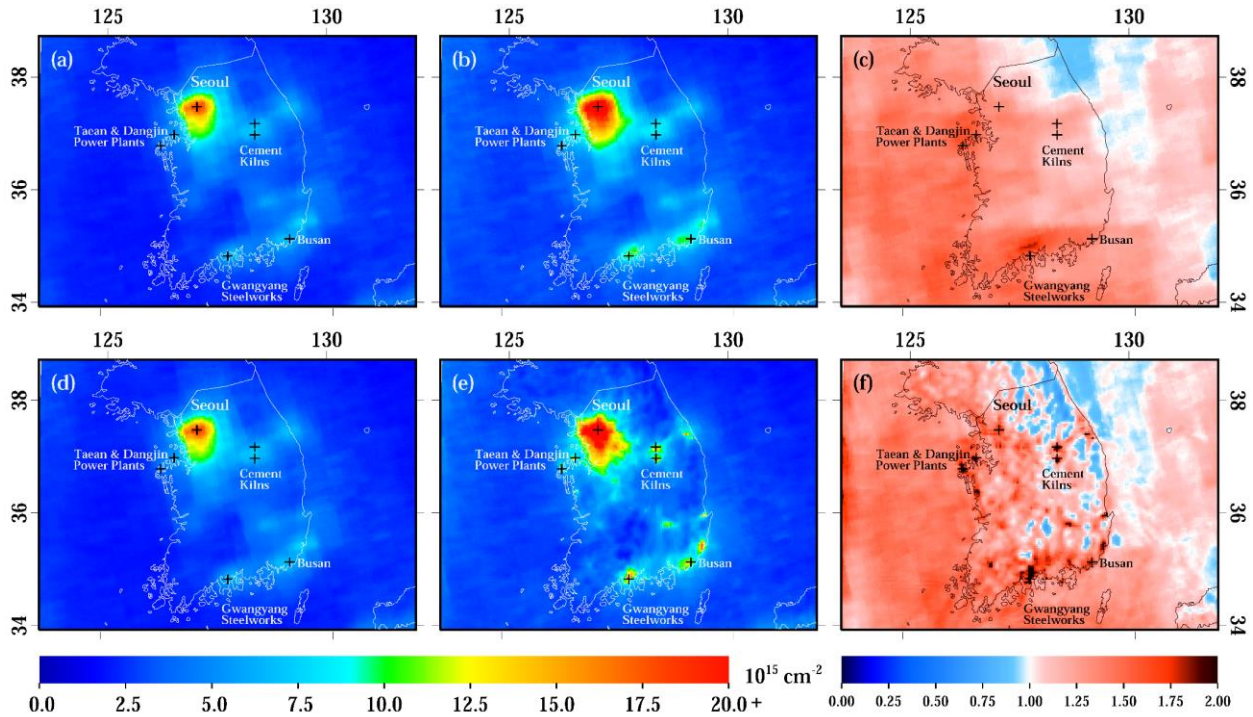


**Figure 2.** (a) OMI-Standard  $\text{NO}_2$  product averaged over a 9-month period, Apr – Jun 2015 – 2017, (b) the OMI-Regional  $\text{NO}_2$  product with only the air mass factor adjustment averaged over the same timeframe, and (c) the ratio between the two products. (d) Same as the top left plot, (e) the OMI-Regional  $\text{NO}_2$  product with the air mass factor adjustment and spatial kernel averaged over the same timeframe, and (f) the ratio between the two products.

10

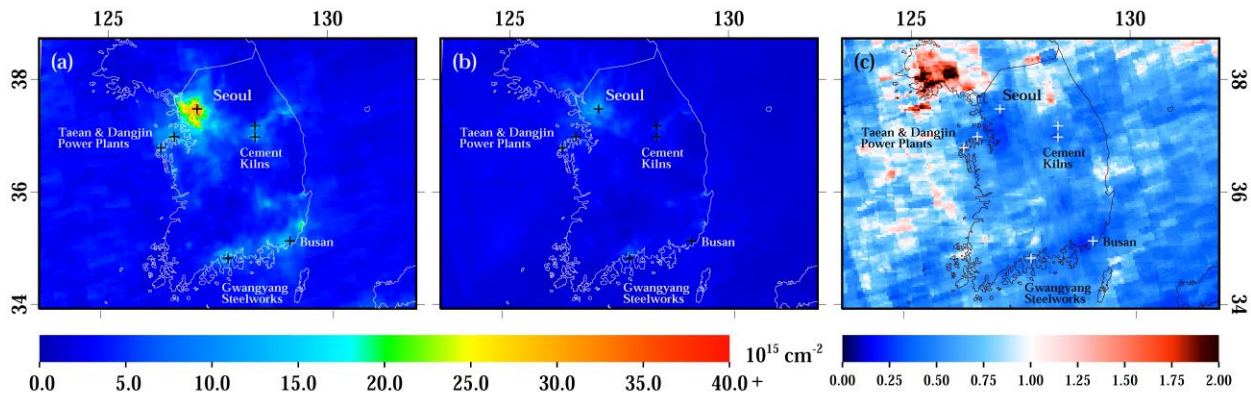


**Figure 3.** (a) The OMI-Regional NO<sub>2</sub> product with the air mass factor adjustment and spatial kernel averaged during the month of May 2016, (b) the WRF-Chem model simulation showing only days with valid OMI measurements, and (c) the ratio between the two products. On average, there are only 9 valid OMI pixels per month observed at any given location on the Korean peninsula during May 2016.

5

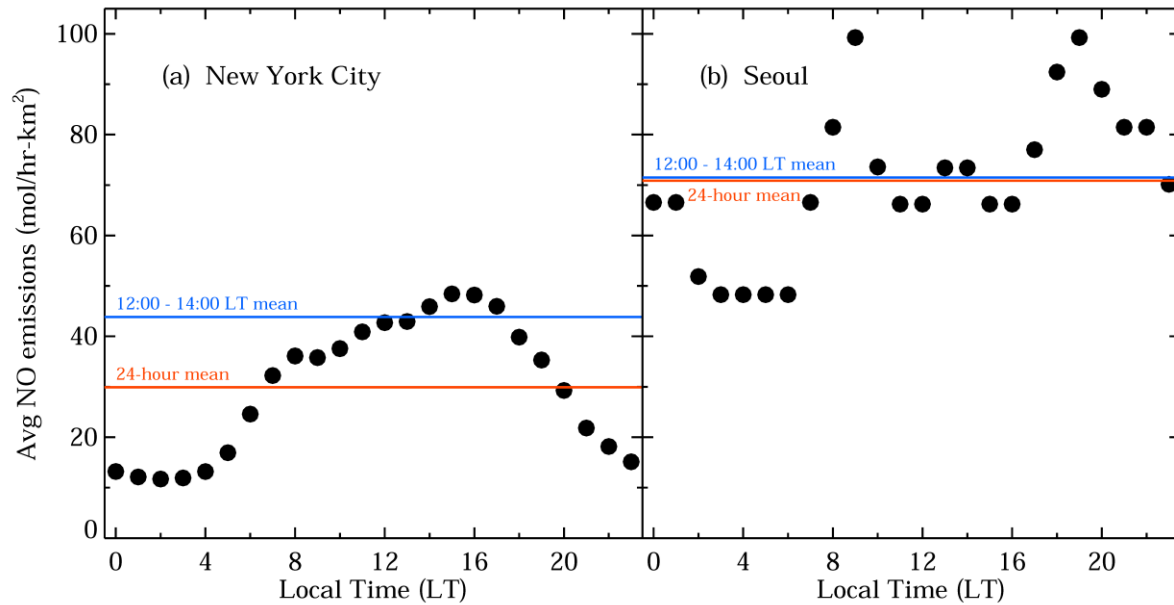


**Figure 4.** The diurnal profile of NO<sub>x</sub> emission rates processed from the bottom-up inventory. (a) The diurnal profile of NO<sub>x</sub> emission rates during a weekday in New York City during July 2011 using SMOKE as the emissions pre-processor (Goldberg et al., 2016). (b) The diurnal profile of emission rates during a weekday in Seoul during May 2016 using EPRES as the emissions pre-processor. Emission profiles in the right panel were used in the WRF-Chem simulation.

10

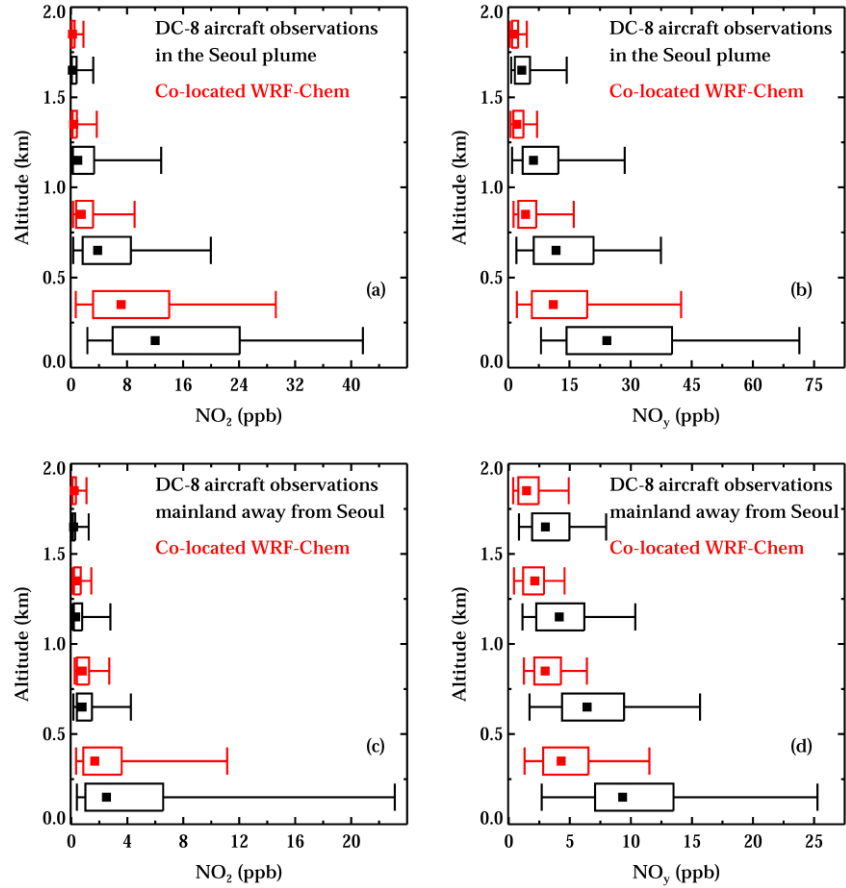
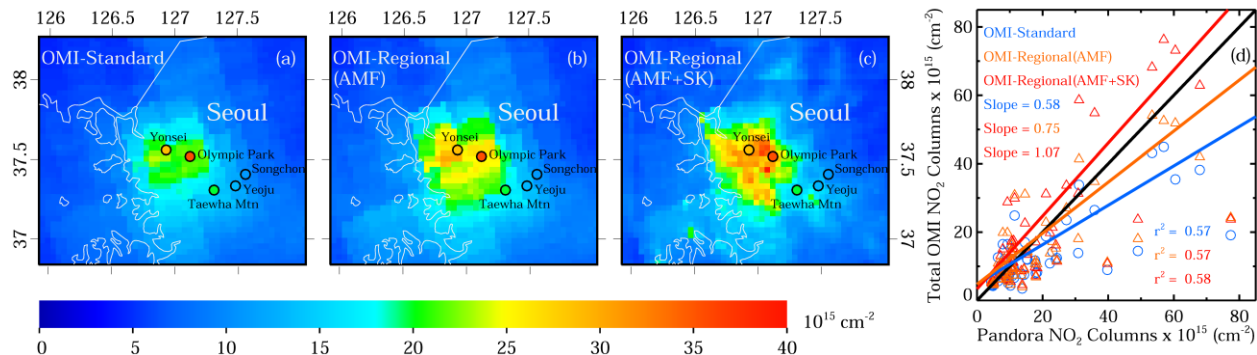


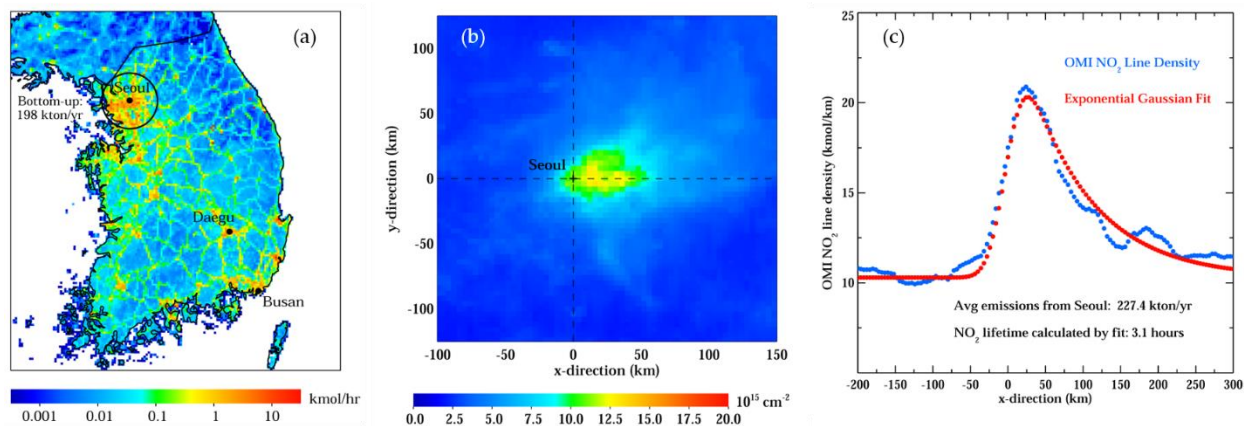
**Figure 5.** Measurements from the DC-8 aircraft binned by altitude in black. Co-located WRF-Chem within the same altitude bin as the aircraft observations are plotted above in red. Square dots represent the median values. Boxes represent the 25<sup>th</sup> and 75<sup>th</sup> percentiles, while whiskers represent the 5<sup>th</sup> and 95<sup>th</sup> percentiles. (a) Comparison of NO<sub>2</sub> in the Seoul plume (SW corner: 37.1° N, 127.05° E, NE corner: 37.75° N, 127.85° E) (b) comparison of NO<sub>y</sub> in the Seoul plume, (c) comparison of NO<sub>2</sub> in areas outside of the Seoul metropolitan area on the Korean peninsula (SW corner: 34.0° N, 126.4° E, NE corner: 37.1° N, 130.0° E), and (d) comparison of NO<sub>y</sub> in areas outside of the Seoul metropolitan area on the Korean peninsula.

5

10



5 **Figure 6.** (a) Total vertical column contents from the OMI-Standard NO<sub>2</sub> product for May 2016, (b) same quantities from the OMI-Regional product with only the air mass factor adjustment (AMF) during the same timeframe, (c) same quantities from the OMI-Regional product with the air mass factor adjustment and spatial kernel (AMF+SK) during the same timeframe, and (d) a comparison between total column contents from the three OMI NO<sub>2</sub> products and Pandora NO<sub>2</sub> during May 2016. An average of Pandora 2-hour means co-located to valid daily OMI overpasses are overlaid in the spatial plots.



10 **Figure 7.** (a) Bottom-up NO<sub>x</sub> emissions inventory compiled for the KORUS-AQ field campaign, (b) the oversampled NO<sub>2</sub> plume rotated based on wind direction for Seoul, Korea from WRF-Chem (4 × 4 km<sup>2</sup>) for May 2016, and (c) NO<sub>2</sub> line densities integrating over the 240 km across plume width (-120 km to 120 km along the y-axis) and the corresponding EMG fit. NO<sub>x</sub> emission estimates are shown in units of kton/yr NO<sub>2</sub> equivalent and represent the mid-afternoon emissions rate.

15

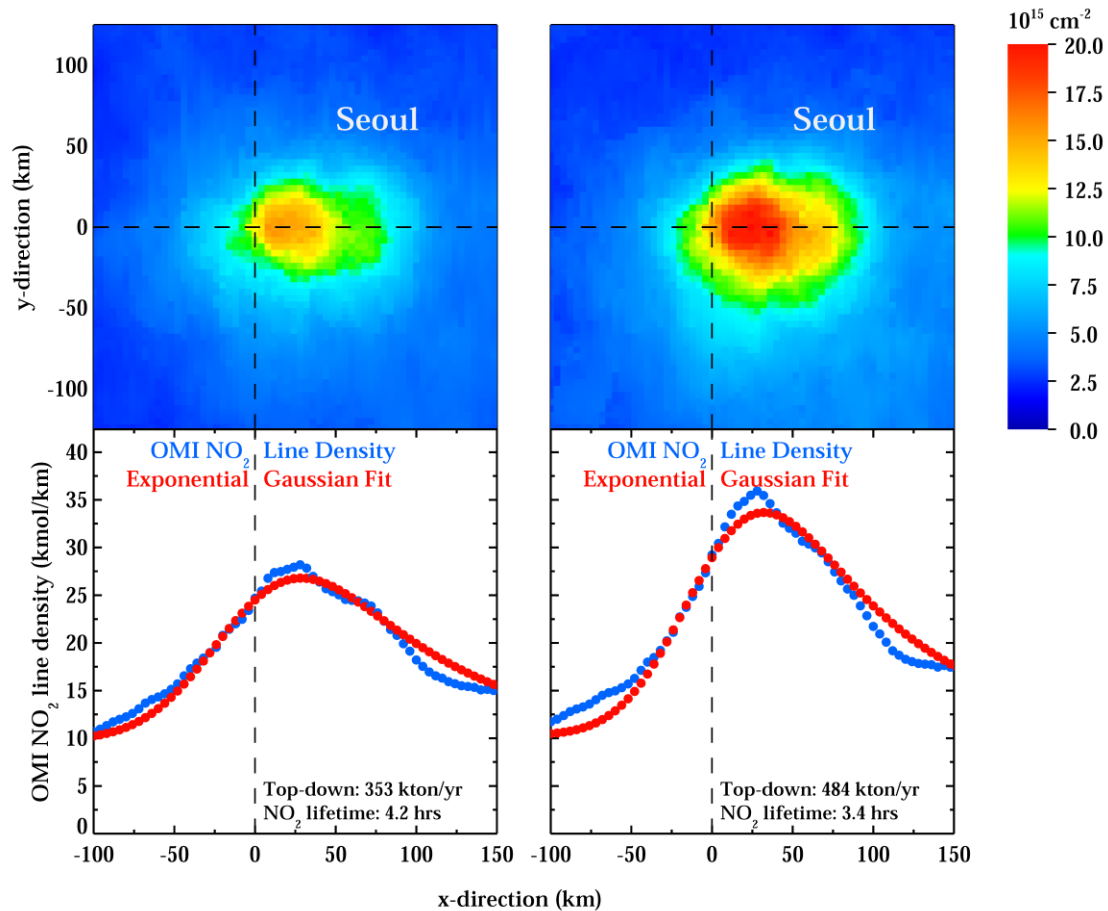


**Figure 8.** Top panels represent the oversampled ( $4 \times 4 \text{ km}^2$ ) OMI  $\text{NO}_2$  plume from Seoul rotated based on wind direction over a 9-month period, Apr – Jun 2015 – 2017, centered on May 2016. Bottom panels represent the OMI  $\text{NO}_2$  line densities integrating over the 240 km across plume width (-120 km to 120 km along the y-axis of the top panels) and the corresponding EMG fit. Left panels are from the OMI-Standard  $\text{NO}_2$  product and right panels are from the OMI-Regional  $\text{NO}_2$  product.  $\text{NO}_x$  emission estimates are shown in units of kton/yr  $\text{NO}_2$  equivalent and represent the mid-afternoon emissions rate.

5

10

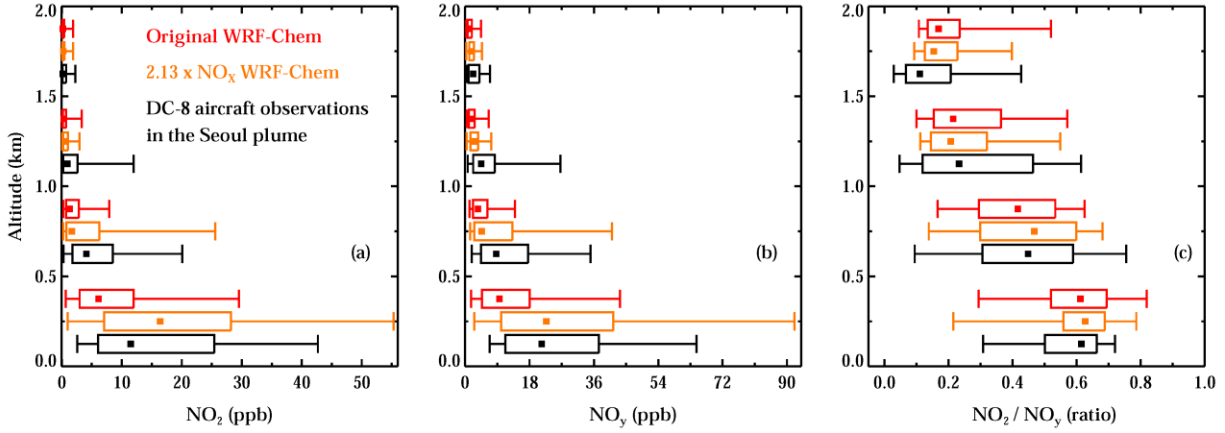


**Figure 9.** Measurements from the DC-8 aircraft binned by altitude in black. Co-located WRF-Chem within the same altitude bin as the aircraft observations are plotted above in red for the original and in orange for the  $2.13 \times \text{NO}_x$  emissions simulation. Square dots represent the median values. Boxes represent the 25<sup>th</sup> and 75<sup>th</sup> percentiles, while whiskers represent the 5<sup>th</sup> and 95<sup>th</sup> percentiles. (a) Comparison of NO<sub>2</sub> in the Seoul plume (SW corner: 37.1° N, 127.05° E, NE corner: 37.75° N, 127.85° E) (b) comparison of NO<sub>y</sub> in the Seoul plume, (c) comparison of the NO<sub>2</sub>-NO<sub>y</sub> ratio in the Seoul plume when coincident NO<sub>2</sub> and NO<sub>y</sub> measurements are available.

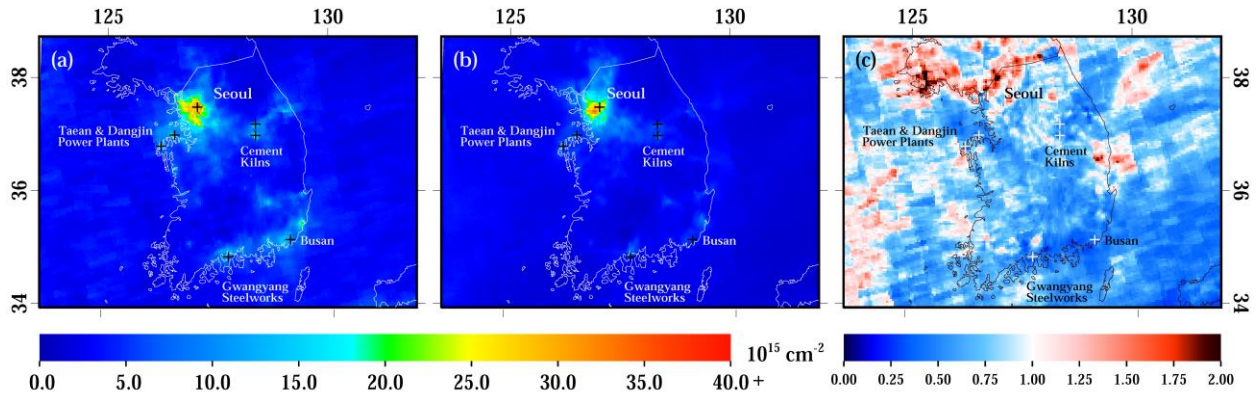


**Figure 10.** Same as Figure 3, but now showing the WRF-Chem simulation with NO<sub>x</sub> emissions in the Seoul metropolitan area increased by a factor of 2.13 in panel (b).

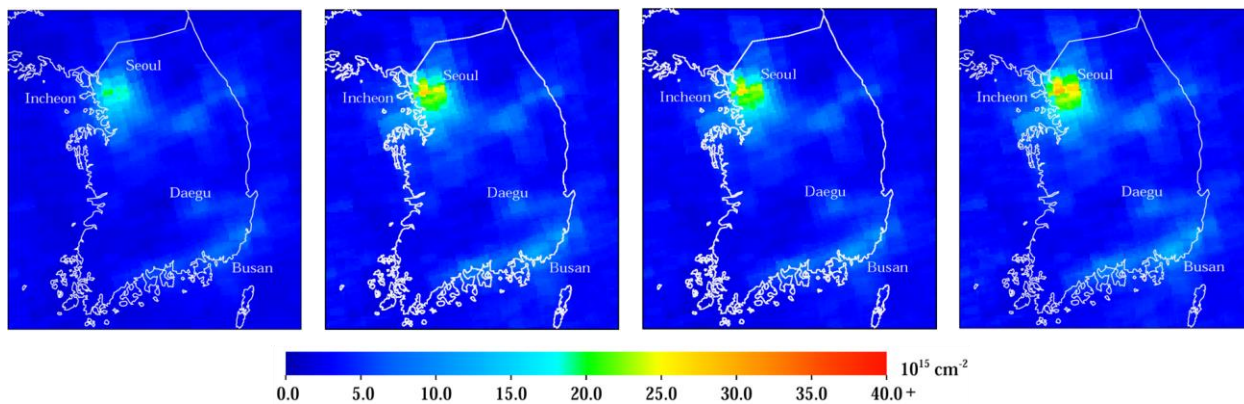


**Figure 11.** (a) The OMI-Standard product during the month of May 2016, (b) the OMI-Regional NO<sub>2</sub> product with the WRF-Chem air mass factor adjustment and spatial kernel during the same period, (c) same as (b) but using WRF-Chem NO<sub>2</sub> profiles scaled based on the aircraft comparison, and (d) same as (b) but using the WRF-Chem simulation with NO<sub>x</sub> in the Seoul metropolitan area emissions increased by a factor of 2.13.

5